

# OTFS-Aided RIS-Assisted SAGIN Systems Outperform Their OFDM Counterparts in Doubly-Selective High-Doppler Scenarios

Chao Xu, *Senior Member, IEEE*, Luping Xiang, *Member, IEEE*, Jiancheng An, Chen Dong, Shinya Sugiura, *Senior Member, IEEE*, Robert G. Maunder, *Senior Member, IEEE*, Lie-Liang Yang, *Fellow, IEEE* and Lajos Hanzo\* *Life Fellow, IEEE*

**Abstract**—The recently-developed reconfigurable intelligent surfaces (RISs) are capable of improving the coverage of space-air-ground integrated networks (SAGINs), where the signals can be reflected in the desired direction without relying on power-thirsty radio-frequency (RF) chains. However, in the face of the substantially increased Doppler frequency, the classic orthogonal frequency-division multiplexing (OFDM) becomes inadequate in supporting RIS for the following reasons. *Firstly*, the detrimental doubly-selective fading leads to inter-symbol interference (ISI) and inter-carrier interference (ICI), which result in error floors for OFDM operating in the time-frequency (TF) domain. *Secondly*, it is far from trivial to configure RIS based on the time-varying fading channels. *Thirdly*, the interpolation-based TF-domain channel estimation methods become impractical for the high-Doppler and high-dimensional RIS systems. Against this background, in this paper, we propose the powerful two-dimensional orthogonal time frequency space (OTFS) modulation for RIS-aided SAGINs, which transforms the time-varying fading encountered in the TF-domain to the time-invariant fading in the delay-Doppler (DD) domain. More explicitly, *first of all*, for the first time in the literature, we devise the DD-domain channel model of RIS assisted SAGINs in the face of doubly-selective fading. *Secondly*, in order to facilitate the RIS configuration in the DD-domain, we propose to create “virtual” Doppler frequencies that guide the phase changes at the RIS, even though the RIS phase rotations do not suffer from Doppler effects. *Thirdly*, we conceive an attractive DD-domain RIS channel estimation method that can support both OFDM and OTFS, where the TF-domain interpolation is eliminated. Our simulation results demonstrate that the proposed DD-domain RIS configuration and channel estimation methods for both OFDM and OTFS are capable of mitigating the error floors encountered in the TF-domain. Furthermore, our simulation results confirm that OTFS-based RIS-assisted SAGIN systems are capable of outperforming their OFDM counterparts and exhibit excellent performance across a wide range of SAGIN channel parameters including the Ricean

**K factor, Doppler frequency, delay spread, coverage distance and carrier frequency.**

**Index Terms**—Reconfigurable intelligent surface, orthogonal time frequency space modulation, space-air-ground, channel estimation, high-mobility, double-selectivity, inter-symbol interference, inter-channel interference, orthogonal frequency-division multiplexing, unmanned aerial vehicle, internet of vehicles.

## I. INTRODUCTION

The fledgling 6G system is envisioned to rely on space-air-ground integrated networks (SAGINs) [1]–[7], which will extend the wireless broadband dividend to a global scale. The International Telecommunication Union (ITU) estimates that only 63% of the world’s population have Internet access, despite the fact that almost 88% have already been covered by the terrestrial 4G/5G systems [8]. Furthermore, the number of Internet-of-Things (IoT) connections has surpassed that of the non-IoT links in 2020, and it is expected that 30 billion IoT devices will have to be connected all over the world by the end of 2025 [9]. However, the operational 4G/5G networks only cover about 20% of terrestrial ground and 5% of the ocean. The time has come for SAGINs to support pervasive broadband services as part of the critical global infrastructure. To make SAGIN a reality, new revolutionary technologies are required for overcoming some of the critical deployment issues. *First of all*, the operational cellular networks have not been designed for supporting high-mobility vehicles, such as satellites, planes, unmanned aerial vehicles (UAVs) as well as trains [10]–[12]. Explicitly, the accurate near-instantaneous knowledge of channel state information (CSI) is essential for supporting wireless links, but the CSI becomes quickly outdated in high-mobility scenarios. *Secondly*, the base station (BS) often has excessively short periods of visibility for high-speed vehicles, planes and satellites. In order to alleviate the extra capital expenditures (CAPEX) and operating expenses (OPEX) of more BSs, the idle devices are often activated for relaying signals between the source and destination in the context of cooperative communications [13]–[15], which inevitably imposes additional delay and power consumption. *Thirdly*, the safety operations of SAGIN applications are of pivotal importance. However, for example, during the maneuvering of an aircraft, the line-of-sight (LoS) may be blocked by the aircraft fuselage, which is also known as the airframe shadowing effect [16]–[19]. This is hazardous because the aircraft may have travelled thousands of meters with a blocked

C. Xu, R. G. Maunder L-L. Yang and L. Hanzo are with the School of Electronics and Computer Science, University of Southampton, Southampton SO17 1BJ, UK (e-mail: {cx1g08,rm,lly,lh}@soton.ac.uk). L. Xiang is with the School of Information and Communication Engineering, University of Electronic Science and Technology of China, Chengdu 611731, China. (e-mail: luping.xiang@uestc.edu.cn). J. An is with the Engineering Product Development Pillar, Singapore University of Technology and Design, Singapore 487372 (e-mail: jiancheng\_an@163.com). C. Dong is with the School of Information and Communication Engineering, Beijing University of Posts and Telecommunications (BUPT), Beijing 100876, China (e-mail:dongchen@bupt.edu.cn). S. Sugiura is with the Institute of Industrial Science, University of Tokyo, Meguro-ku, Tokyo 153-8505, Japan (e-mail: sugiura@ieee.org).

The work of S. Sugiura was supported in part by National Institute of Information and Communications Technology (NICT), Japan. L. Hanzo would like to acknowledge the financial support of the Engineering and Physical Sciences Research Council projects EP/W016605/1 and EP/P003990/1 (CO-ALESCE) as well as of the European Research Council’s Advanced Fellow Grant QuantCom (Grant No. 789028).

control link. Furthermore, the terrestrial shadowing for vehicles, the railway cuttings for high-speed trains [12] and the unfavourable satellite elevation angles [11] may all lead to the diminished LoS. *Finally*, the current 4G/5G modulation of orthogonal frequency-division multiplexing (OFDM) is primarily designed for mitigating the inter-symbol interference (ISI) in time-invariant frequency-selective scenarios [13]. However, often detrimental doubly-selective fading is encountered in the high-mobility SAGIN scenarios, where the substantially increased Doppler frequency leads to inter-carrier interference (ICI) that damages the OFDM's subcarrier (SC) orthogonality.

Against this background, the recently-developed reconfigurable intelligent surfaces (RISs) [20]–[22] have been proposed for improving the coverage of SAGINs without building new BSs, as surveyed in the first section of Table I. The RIS consists of a dense population of passive elements, which reflect the impinging signal to the desired direction without using radio-frequency (RF) chains, hence eliminating both the signal processing delay and the power-consumption of relay nodes. We note that as shown in Table I, the existing RIS assisted SAGINs in the open literature are *mostly limited to the simplified assumption of single-carrier transmission in idealistic time-invariant flat fading channels*. To elaborate, *firstly*, the sum-rate of RIS assisted Internet-of-Vehicles (IoV) was optimized in [23] based on statistical CSI that includes both LoS strength as well as the angle-of-departure/arrival (AoA/AoD). This study was also extended to security outage probability optimization [24], to multi-user scenarios [25] and to IoV scheduling [26]. *Secondly*, in the context of RIS-assisted railway systems, the sum-rate optimization was performed based on both full CSI [27] and statistical CSI [28]. *Thirdly*, the existing RIS assisted UAV communication systems in stationary scenarios have considered energy-efficiency optimization [29], UAV trajectory [30] as well as altitude optimizations [31] plus non-orthogonal multiple access (NOMA) [32]. *Fourthly*, for the case of moving UAVs, RIS-aided decode-and-forward cooperative UAV schemes were proposed in [33], and the related optimization scenarios include TeraHertz (THz) [34], secrecy rate [35] and UAV-aided IoV designs [36]. *Finally*, a range of RIS assisted satellite communication systems have been conceived in [37]–[40], where an ON/OFF-based time-domain (TD) channel estimation technique is conceived in [38].

At the time of writing, *the existing RIS assisted SAGIN systems generally rely on the classic RIS channel estimation methods that are conventionally designed for stationary terrestrial scenarios*, as seen in the second section of Table I, which may be classified into the following four main categories. *First of all*, the LoS based schemes of [41]–[44] configure the RIS purely based on the deterministic LoS knowledge of positioning. *Secondly*, the partially active arrangements of [45]–[47] harness a small number of RF chains in order to estimate a fraction of the RIS links. Then the full channel knowledge is recovered by using compressive sensing and deep learning tools. *Thirdly*, the ON/OFF based least square (LS) schemes of [48], [49] successively estimate the RIS-reflected links one by one without interference, while the LS and the minimum mean squared error (MMSE) methods

of [50]–[52] activate all of the RIS elements based on the classic DFT matrix, so that the direct link and all reflected links become orthogonal. *Fourthly*, the channel estimation overhead can be further reduced by grouping the adjacent RIS elements [48], [59], [60], by compressive sensing [61], [62], deep learning [63] and matrix factorization [53]–[56]. For multi-user RIS systems, a novel three-phase channel estimation method was proposed in [49], which exploited the commonality of the BS-RIS link shared by all users. All of the above RIS channel estimation methods are designed for time-invariant fading channels.

In the face of the doubly-selective fading of SAGIN shown in the third section of Table I, the associated spatial-domain (SD), TD, and frequency-domain (FD) correlations encountered in RIS-assisted UAV systems are modelled in [57], where the RIS configuration is performed based on the idealistic assumption of full CSI knowledge, while the associated waveform and channel estimation technique are not specified. As a further advance, OFDM for RIS-assisted vehicular communication systems in doubly-selective fading is proposed in [58], where the RIS configuration is based on the statistical CSI, while TD and FD interpolation-based channel estimation methods are conceived in order to estimate the time-varying frequency-selective TF-domain fading channels.

In recent years, the two-dimensional orthogonal time frequency space (OTFS) modulation [64]–[66] has attracted substantial research interests as a benefit of its superior performance over OFDM in doubly-selective fading channels. More explicitly, OTFS modulates the information symbols in the delay-Doppler (DD) domain instead of the conventional time-frequency (TF) domain [67]–[69]. On one hand, by invoking the symplectic finite Fourier transform (SFFT), the OTFS symbols are spread over the entire TF-domain, which offers the potential of exploiting the full channel diversity [70]–[72]. On the other hand, the OTFS transforms the time-varying TF-domain fading model into time-independent DD-domain representation of the channel parameters, including the fading gain, Doppler frequency and delay of each resolvable propagation path. As a result, the DD-domain channel estimation [73], [74] no longer suffers from time-varying ISI in the TD or from the Doppler-induced ICI in the FD, rendering a truly robust delay-resilience and Doppler-resilience for SAGIN applications. Low-complexity equalization techniques have been proposed for OTFS in [75], [76]. Furthermore, by exploiting the sparsity of the DD-domain fading matrix, message passing (MP) detectors are conceived in [77]–[79].

In summary, the classic OFDM operating in the TF-domain becomes inadequate in supporting RIS assisted SAGINs for the following reasons:

- I) **System Modelling:** The detrimental doubly-selective fading leads to ISI in the TD and ICI in the FD, which inevitably result in error floors for OFDM relying on subcarrier orthogonality.
- II) **RIS Configuration:** It is far from trivial to instantaneously feed back the control signals and configure the RIS based on the time-varying frequency-selective TF-domain fading channels.

TABLE I: State-of-the-art RIS-assisted SAGIN systems.

	Scenarios	Waveform	RIS configuration	Channel model	Channel estimation	Related publications
Chen <i>et al.</i> [23]	Car	Single-carrier	Sum rate optimization based on statistical CSI	Time-invariant flat fading	Not specified	[24] maximized security outage probability for RIS-assisted IoV; [25] extended to RIS-assisted multi-user IoV; [26] jointly optimized IoV scheduling and RIS configuration.
Xu <i>et al.</i> [27]	Train	Single-carrier	Sum rate optimization based on full CSI	Time-invariant flat fading	Not specified	[28] performed sum rate optimization based on statistical CSI.
Diamanti <i>et al.</i> [29]	Stationary UAV	Single-carrier	Energy-efficiency optimization based on full CSI	Time-invariant flat fading	Not specified	[30] jointly optimized trajectory and RIS configuration; [31] optimized the altitudes RIS-carrying UAVs; [32] optimized UAV trajectory for RIS-assisted NOMA.
Yang <i>et al.</i> [33]	UAV	Single-carrier	RIS and decode-and-forward optimization based on full CSI	Time-invariant flat fading	Not specified	[34] maximized sum rate based on full CSI in THz; [35] maximized secrecy rate based on full CSI; [36] invoked RIS to assist UAV-aided IoV.
Tekbilyik <i>et al.</i> [37]	Satellite	Single-carrier	Max-SNR based on full CSI	Time-invariant flat fading	Not specified	[38] performed ON/OFF-based TD channel estimation; [39] proposed RIS-carrying UAV for enhancing satellite link; [40] optimized sum rate for RIS-assisted satellite communication based on full CSI.
Han <i>et al.</i> [41]	Stationary terrestrial	Single-carrier	Max-SNR based on statistical CSI	Time-invariant flat fading	LoS knowledge	[42] conceived hybrid beamforming at the BS based on LoS; [43] invoked discrete-phase RIS; [44] conceived RIS-assisted joint localization and communication.
Taha <i>et al.</i> [45]	Stationary terrestrial	Single-carrier	Max-SNR based on full CSI	Time-invariant flat fading	Partially active RIS with compressive sensing	[46] extended to multi-carrier systems; [47] investigated the RIS hardware architecture using minimum active elements for channel estimation.
Yang <i>et al.</i> [48]	Stationary terrestrial	OFDM	Max-rate based on full CSI	Time-invariant freq.-selective	ON/OFF-based FD channel estimation	[49] extended to multiuser; [50], [51] invoked DFT-based RIS pattern; [52] incorporated BS beamforming.
He <i>et al.</i> [53]	Stationary terrestrial	Single-carrier	Random configuration	Time-invariant flat fading	ON/OFF-based with matrix factorization	[54] extended to multiuser MIMO; [55], [56] invoked parallel factor decomposition channel estimation; [49] exploited the commonality of the BS-RIS link shared by all users.
Xiong <i>et al.</i> [57]	UAV	Not specified	Max-SNR based on full CSI	Doubly-selective	Not specified	
Xu <i>et al.</i> [58]	Car, UAV	OFDM	Max-SNR based on statistical CSI	Doubly-selective	FD/TD domains interpolation	
This work	SAGIN	OTFS, OFDM	Max-SNR based on statistical CSI	Doubly-selective	DD-domain without interpolation	

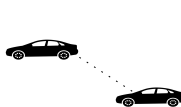




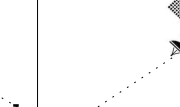
						
	Vehicle-to-Vehicle	Train	Civil Aviation	Supersonic UAV	Hypersonic UAV	Low Earth Orbit
Distance	300 m	500 m	10 km	20 km	20 km	2000 km
Speed	100 mph	336 mph	671 mph	Mach 3	Mach 12	Mach 25
Ricean K	$K^{SD} = -3$ dB $K^{SR} = -3$ dB $K^{RD} = 3$ dB	$K^{SD} = -3$ dB $K^{SR} = -3$ dB $K^{RD} = 3$ dB	$K^{SD} = 3$ dB $K^{SR} = 3$ dB $K^{RD} = 6$ dB	$K^{SD} = -3$ dB $K^{SR} = -3$ dB $K^{RD} = 6$ dB	$K^{SD} = -3$ dB $K^{SR} = -3$ dB $K^{RD} = 6$ dB	$K^{SD} = 2$ dB $K^{SR} = 2$ dB $K^{RD} = 6$ dB
$\tau_{max}$	FR1: 4000 ns FR2: 800 ns	FR1: 4000 ns FR2: 800 ns	FR1: 600 ns FR2: 250 ns	FR1: 600 ns FR2: 250 ns	FR1: 400 ns FR2: 120 ns	FR1: 100 ns FR2: 40 ns
$\Delta f$	FR1: 15 kHz FR2: 60 kHz	FR1: 15 kHz FR2: 120 kHz	FR1: 30 kHz FR2: 240 kHz	FR1: 60 kHz FR2: 960 kHz	FR1: 240 kHz FR2: 3840 kHz	FR1: 480 kHz FR2: 7680 kHz

Fig. 1: Summary of the SAGIN (worst-case) scenarios considered in this paper.

**III) Channel Estimation:** The high-complexity interpolation-based TF-domain channel estimation techniques become impractical and inaccurate for the high-Doppler and high-dimensional RIS assisted SAGIN systems.

Against this background, in this paper, we propose to facilitate OTFS-based RIS-assisted SAGINs, which aim for transforming the time-varying TF-domain RIS-reflected fading channels to the time-invariant DD-domain, where the following open problems are solved for the first time in the literature, as highlighted in Table II:

**I) System Modelling:** How to model the DD-domain RIS-

reflected fading channels?

**II) RIS Configuration:** How to configure the RIS in the DD-domain?

**III) Channel Estimation:** How to facilitate the DD-domain RIS channel estimation?

In more detail, the novel contributions of this work are as follows:

**I) System Modelling:** We propose to model the doubly-selective fading channels of RIS-assisted SAGINs in both the TF-domain and DD-domain, where *both OFDM and OTFS can be supported in a unified platform*. Further-

TABLE II: State-of-the-art RIS channel estimation techniques.

	Channel estimation methods	RIS modelling			Doubly-Selectivity		OTFS Upgrade			
		Passive RIS	Both direct and reflected links	Both LoS and NLoS	Freq Selectivity	Time Selectivity	DD domain channel model	DD domain RIS configuration	DD domain channel estimation	Support both OFDM and OTFS
Han <i>et al.</i> [41]	LoS knowledge	✓	✓	✓						
Taha <i>et al.</i> [45]	Compressive sensing deep learning				✓					
Yang <i>et al.</i> [48]	ON/OFF-based LS	✓	✓	✓	✓					
Wang <i>et al.</i> [49]	ON/OFF-based LS	✓	✓	✓						
Jensen <i>et al.</i> [50]	DFT-based LS	✓	✓							
Zheng <i>et al.</i> [51]	DFT-based LS	✓	✓	✓	✓					
Nadeemet <i>et al.</i> [52]	DFT-based MMSE	✓	✓	✓						
You <i>et al.</i> [60]	DFT-based LS	✓		✓						
Chen <i>et al.</i> [62]	Compressive sensing	✓								
Ma <i>et al.</i> [63]	Deep learning	✓		✓						
He <i>et al.</i> [53]	Matrix factorization	✓								
Liu <i>et al.</i> [54]	Matrix factorization	✓	✓	✓						
Xu <i>et al.</i> [58]	MMSE in FD/TD	✓	✓	✓	✓	✓				
This work	DD-domain	✓	✓	✓	✓	✓	✓	✓	✓	✓

more, the salient SAGIN characteristics considered in this paper are summarized in Fig. 1, which take into account the most challenging SAGIN propagation conditions in vehicle-to-vehicle (V2V) scenarios, in high-speed trains operating in railway cuttings [12], the airframe shadowing effect of airplanes and UAVs [16]–[19] as well as the unfavourable elevation angles of the low earth orbit (LEO) satellites [11]. We will demonstrate that the proposed DD-domain RIS configuration and channel estimation methods are capable of achieving reliable performance across a wide range of SAGIN channel parameters.

**II) RIS Configuration:** In order to configure the RIS in the DD-domain, we propose to define the time-varying RIS phase rotations by the equivalent time-invariant phase parameters and the equivalent “virtual” Doppler frequencies, *which are created to guide the phase changes at the RIS*, even though the RIS phase rotations do not experience Doppler effects. In this way, the RIS is configured to tune the phase and Doppler differences between the direct link and the RIS-reflected links in the DD-domain, so that the LoS power is maximized at the destination. The proposed RIS configuration opts for relying on the statistical CSI as widely assumed in [25], [41]–[44], [80]–[83], which eliminates the need for performing CSI estimation at the RIS.

**III) Channel Estimation:** As a further advance, we conceive a DD-domain RIS channel estimation technique that can be invoked by both OFDM and OTFS, where *the TF-domain interpolation is eliminated*. This new DD-domain signal processing technique conceived for RIS systems facilitates the following breakthroughs:

- The proposed DD-domain RIS configuration and channel estimation techniques can support both OFDM and OTFS, where *the error floors observed in their RIS counterparts operating in the TF-domain are mitigated*.
- The proposed DD-domain RIS operations are capable of substantially improving the performance of SAGINs *across a wide range of SAGIN channel parameters* including the Ricean K factor, Doppler frequency, delay spread, coverage distance and carrier frequency.

- Our simulation results demonstrate that the proposed OTFS aided RIS assisted SAGIN systems are capable of *substantially outperforming their OFDM counterparts* in terms of BER, achievable rate and coverage distance.

The following notations are used throughout the paper. The operations  $(\cdot)^*$  and  $(\cdot)^H$  denote the conjugate of a complex number and the Hermitian transpose of a complex matrix, respectively. The notations  $\ln(\cdot)$  and  $\exp(\cdot)$  refer to the natural logarithm and natural exponential functions, respectively. The notations  $p(\cdot)$  and  $E(\cdot)$  represent the probability and the expectation, respectively, while  $\mathbf{a} \in \mathcal{C}^{N \times 1}$  refers to a complex-valued vector of size  $(N \times 1)$ , and  $\mathbf{A} \in \mathcal{C}^{c \times d}$  denotes that  $\mathbf{A}$  is a complex-valued matrix of size  $(c \times d)$ .

This paper is organized as follows. The TD and DD channel modelling of RIS assisted SAGINs is conceived in Sec. II. The optimization of RIS reflection coefficients is formulated and solved in Sec. III. Our bespoke channel estimation techniques are proposed in Sec. IV, while our simulation results are presented in Sec. V. Finally, our conclusions are offered in Sec. VI.

## II. TD AND DD CHANNEL MODELLING OF RIS ASSISTED SAGINs

### A. General Modelling Notations

In this paper, a single antenna is used both at the source and at the destination, which minimizes the CSI estimation overhead in the high-mobility scenarios considered. We note that as the numbers of antennas is increased at the BS and/or the user, the channel estimation scheme conceived in this paper can be directly applied using an ON/OFF pattern of antennas. However, this results in an excessive pilot overhead for high-dimensional RIS links that grows with the number of antennas, which is not preferred in high-mobility scenarios. Furthermore, to elaborate a little further on the scenarios considered in Fig. 1, these scenarios are associated with very different distances, speed, Ricean K factor and maximum delay  $\tau_{\max}$ . The source-destination (SD), source-RIS (SR) and RIS-destination (RD) links are assumed to be more sparse in the 5G mmWave frequency range 2 (FR2) than in FR1 [5], [10]–[12]. The subcarrier spacing (SCS)  $\Delta f$  in Fig. 1 is

TABLE III: OFDM and OTFS notations.

	TD	FD	DD
Transmitter	$s_{n,m}$	$\bar{s}_{n,m}$	$\tilde{s}[k,l]$
Fading	$h_{n,m,l}$	$\bar{h}_{n,m}$	$\tilde{h}_p \omega_{MN}^{k_p(nM+m-l_p)}$
Receiver	$y_{n,m}$	$\bar{y}_{n,m}$	$\tilde{y}[k,l]$

specifically chosen for the sake of supporting effective DD-domain channel estimation.

For the OFDM and OTFS representations, the TD, FD and DD notations follow the generic rules exemplified in Table III. An OTFS frame may also be viewed as an Inverse SFFT (ISFFT) precoding applied to  $N$  consecutive OFDM symbols having  $M$  subcarriers. The TD signal received in the face of doubly-selective fading is modelled as [64]–[66]:

$$y(t) = \int \int \tilde{h}(\tau, \vartheta) s(t - \tau) e^{j2\pi\vartheta(t-\tau)} d\tau d\vartheta + v(t) \Big|_{t=\frac{nT}{M} = \frac{n}{M\Delta f}}, \quad (1)$$

where  $\tau$  and  $\vartheta$  refer to the delay and Doppler frequency, while  $s(t)$  and  $v(t)$  denote the TD transmitted signal and additive white Gaussian noise (AWGN). The corresponding OFDM symbol period is  $T = \frac{1}{\Delta f}$ , where  $\Delta f$  refers to the subcarrier spacing (SCS). The DD-domain fading gain in (1) is expressed as:

$$\tilde{h}(\tau, \vartheta) = \sum_{p=0}^{P-1} \tilde{h}_p \delta(\tau - \tau_p) \delta(\vartheta - \vartheta_p) \Big|_{\tau_p = \frac{l_p T}{M\Delta f}, \vartheta_p = \frac{k_p}{NT}}. \quad (2)$$

On one hand, when the maximum delay exceeds the sampling period, i.e. we have  $\tau_{\max} > \frac{T}{M}$ , frequency-selectivity is encountered, which imposes ISI in the TD. It is assumed in (2) that a total of  $P$  resolvable paths of the DD-domain fall into  $L$  time delay line (TDL) taps in the TD, i.e. we have  $\tau_p = \frac{l_p T}{M} = \frac{l_p}{M\Delta f}$ , where  $l_p \in [0, L-1]$ . On the other hand, when the maximum Doppler frequency  $f_D$  becomes comparable to the SCS  $\Delta f$ , time-selectivity is encountered, which imposes ICI in the FD. It is assumed in (2) that the component Doppler frequencies are all substantially lower than the overall bandwidth, i.e. we have  $\{\vartheta_p \ll M\Delta f\}_{p=0}^{P-1}$ , so that  $\tilde{h}_p e^{\frac{j2\pi\vartheta_p n}{M\Delta f}}$  still remains near-constant over a sampling period of  $\frac{T}{M}$ , but varies for  $n = 0, \dots, M-1$  within an OFDM symbol period  $T$ . Upon sampling in the DD-domain, the time-varying frequency-selective fading can be uniquely represented by the time-invariant parameters of fading gain  $\tilde{h}_p$ , Doppler index  $k_p$  and delay index  $l_p$ . The relationship between the TD and DD fading representations seen in Table III is expressed as:

$$h_{n,m,l} = \sum_{p=0}^{P-1} \tilde{h}_p \omega_{MN}^{k_p(nM+m-l_p)} \mathfrak{b}(k_p, l_p) \Big|_{l=l_p}, \quad (3)$$

where  $\omega_{MN}^{k_p(nM+m-l_p)} = \exp(j\frac{2\pi k_p(nM+m-l_p)}{MN})$  and  $h_{n,m,l}$  models the  $l$ -th TDL tap for the  $m$ -th sample in the  $n$ -th OFDM symbol, while we have  $\mathfrak{b}(k_p, l_p) = 1|_{l=l_p}$  or  $\mathfrak{b}(k_p, l_p) = 0|_{l \neq l_p}$  for the cases that the  $p$ -th DD-domain resolvable path falls into the  $l$ -th TDL tap, or otherwise, respectively. This implies that the DD-domain representation allows us to separate the propagation paths experiencing the same delay, hence attaining a higher degree of freedom in channel modelling. Nonetheless, it is worth noting that the off-the-grid paths associated with fractional delay and Doppler indices may induce interference, which can be mitigated by appropriate windowing at the transmitter and receiver in order

to enhance the channel sparsity in the DD-domain [69]. Furthermore, it is proven in [66] from first principles that the DD-domain interferences induced by the fractional indices become negligible, given sufficient time duration and bandwidth, which is the general assumption of this paper.

### B. Large-Scale Path Loss and Small-Scale Fading Modelling

The path loss (PL) and small-scale fading parameters are summarized in Table IV. The PL of each link is given by [5], [84]–[89]:

$$\text{PL} = -10\gamma \log_{10}(d) - 20 \log_{10} \left( \frac{4\pi}{\lambda} \right) + G_e = 10 \log_{10} \Gamma \text{ dB}, \quad (4)$$

where  $\gamma$  denotes the PL exponent (PLE). The effective antenna gain is formulated as ( $G_e = \frac{4\pi A_e}{\lambda^2}$ ), where  $A_e$  refers to the antenna aperture of the transmitter or the receiver, while  $f_c$  and  $\lambda = \frac{c}{f_c}$  refer to the carrier frequency and the wavelength, respectively. The distance  $d$  is evaluated in real-time based on the coordinates of the source ( $x_S, y_S, z_S$ ), of the RIS ( $x_R, y_R, z_R$ ) and of the destination ( $x_D, y_D, z_D$ ). For example, the distance of the SD link is evaluated by [ $d^{\text{SD}} = \sqrt{(x_S - x_D)^2 + (y_S - y_D)^2 + (z_S - z_D)^2}$ ]. The non-logarithmic PL is given by  $\Gamma$ , which is updated based on the distance. In summary, the PL of (4) is a function of distance and carrier frequency/wavelength, which allows us to examine the performance of RIS-assisted high-mobility systems in different frequency bands. Specifically, assuming the same PLE for the SR and RD links as  $\gamma^{\text{SRD}} = \gamma^{\text{SR}} = \gamma^{\text{RD}}$ , the overall PL of the cascaded source-RIS-destination channel is given by  $\Gamma^{\text{SRD}} = \Gamma^{\text{SR}} \Gamma^{\text{RD}} \propto \frac{1}{(d^{\text{SR}} d^{\text{RD}})^{\gamma^{\text{SRD}}}}$ . This implies that under generic far-field propagation conditions, the RIS-reflected links suffer from severe PL that is inversely proportional to the product of the segment distances [90]–[92].

For small-scale fading, the LoS path is always associated with  $l = 0$ , while the NLoS paths are randomly distributed over  $L^i$  TDL taps for  $i = \text{SD/SR/RD}$ . The LoS and NLoS powers are determined by the Ricean K factor  $K^i$  for  $i = \text{SD/SR/RD}$ . The maximum Doppler frequency is given by  $f_D^i = \frac{v^i f_c}{c}$  for  $i = \text{SD/SR/RD}$ , where  $c$ ,  $f_c$  and  $v^i$  refer to the speed of light, carrier frequency and the vehicular speed, respectively. The RIS is assumed to be comprised of  $R$  passive reflecting elements, where a uniform planar array (UPA) is adopted. The RIS phase rotations are also assumed to be time-varying as  $\alpha_{n,m} = [\alpha_{n,m}^1, \dots, \alpha_{n,m}^R]^T$ , where we have the constant-envelope constraint of  $\{|\alpha_{n,m}^r| = 1\}_{r=1}^R$ . Nonetheless, we note that due to the passive nature of RISs, the same phase rotation of each RIS element will be applied to all the channel impulse response (CIR) taps in the TD or equivalently to the channel frequency response (CFR) of all SCs in the FD. In other words, the RIS phase rotations can be time-varying but remain strictly non-frequency-selective. As a result, in this work, we opt for configuring the RIS based on statistical CSI, which will be elaborated on in Sec III.

### C. The Source-Destination (SD) Link

For the SD link, there are  $P^{\text{SD}}$  DD-domain resolvable paths associated with the maximum delay of  $\tau_{\max}^{\text{SD}}$ . The TD and DD-

TABLE IV: Key model parameters of RIS-assisted system.

	Source-Destination (SD) Link	Source-RIS (SR) Link	RIS-Destination (RD) Link
Distance	$d^{\text{SD}} = \sqrt{(x_S - x_D)^2 + (y_S - y_D)^2 + (z_S - z_D)^2}$	$d^{\text{SR}} = \sqrt{(x_S - x_R)^2 + (y_S - y_R)^2 + (z_S - z_R)^2}$	$d^{\text{RD}} = \sqrt{(x_R - x_D)^2 + (y_R - y_D)^2 + (z_R - z_D)^2}$
PLE	$\gamma^{\text{SD}}$	$\gamma^{\text{SR}}$	$\gamma^{\text{RD}}$
PL	$\Gamma^{\text{SD}} = (d^{\text{SD}})^{-\gamma^{\text{SD}}} \frac{4\pi}{\lambda}^{-2} 10^{0.1(G_e^{\text{Tx}} + G_e^{\text{Rx}})}$	$\Gamma^{\text{SR}} = (d^{\text{SR}})^{-\gamma^{\text{SR}}} \frac{4\pi}{\lambda}^{-2} 10^{0.1G_e^{\text{Tx}}}$	$\Gamma^{\text{RD}} = (d^{\text{RD}})^{-\gamma^{\text{RD}}} \frac{4\pi}{\lambda}^{-2} 10^{0.1G_e^{\text{Rx}}}$
Ricean factor	$K^{\text{SD}}$	$K^{\text{SR}}$	$K^{\text{RD}}$
LoS power	$\frac{K^{\text{SD}}}{K^{\text{SD}} + 1}$	$\frac{K^{\text{SR}}}{K^{\text{SR}} + 1}$	$\frac{K^{\text{RD}}}{K^{\text{RD}} + 1}$
NLoS power	$\frac{1}{(K^{\text{SD}} + 1)}$	$\frac{1}{(K^{\text{SR}} + 1)}$	$\frac{1}{(K^{\text{RD}} + 1)}$
Max. Doppler	$f_D^{\text{SD}}$	$f_D^{\text{SR}}$	$f_D^{\text{RD}}$
Max. Delay	$\tau_{\text{max}}^{\text{SD}}$	$\tau_{\text{max}}^{\text{SR}}$	$\tau_{\text{max}}^{\text{RD}}$
LoS offset	$f_D^{\text{SD}} \cos(\phi_0^{\text{SD}})$	$f_D^{\text{SR}} \cos(\phi_0^{\text{SR}})$	$f_D^{\text{RD}} \cos(\phi_0^{\text{RD}})$
LoS AoA	$\phi_0^{\text{SD}} = \arctan \frac{y_S - y_D}{x_S - x_D}$	$\phi_0^{\text{SR}} = \arctan \frac{y_S - y_R}{x_S - x_R}$	$\phi_0^{\text{RD}} = \arctan \frac{y_R - y_D}{x_R - x_D}$
RIS AoA		$\theta_R^{\text{AoA}} = \arccos \frac{z_S - z_R}{d^{\text{SR}}}$ , $\varphi^{\text{AoA}} = \arctan \frac{y_S - y_R}{x_S - x_R}$	
RIS AoD			$\theta_R^{\text{AoD}} = \arccos \frac{z_D - z_R}{d^{\text{RD}}}$ , $\varphi^{\text{AoD}} = \arctan \frac{y_D - y_R}{x_D - x_R}$

domain fading representations of the  $l$ -th TDL tap of the  $m$ -th TD sampling period within the  $n$ -th OFDM symbol is given by:

$$h_{n,m,l}^{\text{SD}} = \sum_{p=0}^{P^{\text{SD}}-1} \tilde{h}_p^{\text{SD}} \omega_{MN}^{k_p^{\text{SD}}(nM+m-l_p)} \mathfrak{b}(k_p^{\text{SD}}, l_p)|_{l=l_p}, \quad (5)$$

for  $0 \leq l \leq L^{\text{SD}} - 1$ . More explicitly, for the NLoS associated with  $1 \leq p \leq P^{\text{SD}} - 1$ , the time-invariant gain  $\tilde{h}_p^{\text{SD}}$  is generated based on the complex Gaussian distribution with zero mean and a variance of  $\frac{1}{(K^{\text{SD}}+1)(P^{\text{SD}}-1)}$ . The NLoS delay indices  $\{l_p\}_{p=1}^{P^{\text{SD}}-1}$  are randomly generated within  $[0, L^{\text{SD}} - 1]$ , where we have  $L^{\text{SD}} = \lceil \tau_{\text{max}}^{\text{SD}} M \Delta f \rceil$ . The Doppler indices  $\{k_p^{\text{SD}}\}_{p=1}^{P^{\text{SD}}-1}$  are randomly generated over the range of  $[-k_{\text{max}}^{\text{SD}}, k_{\text{max}}^{\text{SD}}]$ , where the maximum index is given by  $k_{\text{max}}^{\text{SD}} = \lceil f_D^{\text{SD}} NT \rceil$ . Furthermore, the LoS path associated with  $l = l_p = 0$  and  $p = 0$  is given by:

$$h_{n,m,0}^{\text{SD}} = \sqrt{\frac{K^{\text{SD}}}{K^{\text{SD}} + 1}} \omega_{MN}^{k_0^{\text{SD}}(nM+m)}, \quad (6)$$

where the LoS fading gain  $\tilde{h}_0^{\text{SD}}$  of (5) associated with  $p = 0$  is simply given by  $\tilde{h}_0^{\text{SD}} = \sqrt{\frac{K^{\text{SD}}}{K^{\text{SD}} + 1}}$ , while the LoS Doppler index is given by  $k_0^{\text{SD}} = \lceil f_D^{\text{SD}} \cos(\phi_0^{\text{SD}}) NT \rceil$ . The angle between the LoS and the direction of movement is evaluated by  $(\phi_0^{\text{SD}} = \arctan \frac{y_S - y_D}{x_S - x_D})$ .

As a result, the signal received from the direct SD link is modelled in the TD and DD-domain as follows:

$$y_{n,m}^{\text{SD}} = \sum_{l=0}^{L^{\text{SD}}-1} h_{n,m,l}^{\text{SD}} s_{n,m-l} = \sum_{p=0}^{P^{\text{SD}}-1} \tilde{h}_p^{\text{SD}} \omega_{MN}^{k_p^{\text{SD}}(nM+m-l_p)} s_{n,m-l_p}, \quad (7)$$

where we have  $\mathfrak{b}(k_p^{\text{SD}}, l_p) = 1$  for all the  $P^{\text{SD}}$  resolvable paths.

#### D. The Source-RIS (SR) Link

The SR link has  $P^{\text{SR}}$  resolvable paths and a maximum delay of  $\tau_{\text{max}}^{\text{SR}}$ . Similar to (5), the NLoS path for the  $r$ -th RIS element ( $1 \leq r \leq R$ ) is modelled by:

$$h_{n,m,l}^{\text{SR}_r} = \sum_{p=0}^{P^{\text{SR}}-1} \tilde{h}_p^{\text{SR}_r} \omega_{MN}^{k_p^{\text{SR}_r}(nM+m-l_p)} \mathfrak{b}(k_p^{\text{SR}_r}, l_p)|_{l=l_p}, \quad (8)$$

for  $0 \leq l \leq L^{\text{SR}} - 1$ , where the NLoS power of  $\{\tilde{h}_p^{\text{SR}_r}\}_{p=1}^{P^{\text{SR}}-1}$  is updated to  $\frac{1}{(K^{\text{SR}}+1)(P^{\text{SR}}-1)}$ . The ranges for the delay and Doppler indices are given by  $l_p \in [0, L^{\text{SR}} - 1]$  and

$k_p^{\text{SR}_r} \in [-k_{\text{max}}^{\text{SR}}, k_{\text{max}}^{\text{SR}}]$ , respectively, where we have  $L^{\text{SR}} = \lceil \tau_{\text{max}}^{\text{SR}} M \Delta f \rceil$  and  $k_{\text{max}}^{\text{SR}} = \lceil f_D^{\text{SR}} NT \rceil$ . Furthermore, based on the azimuth and elevation AoAs of  $\theta^{\text{AoA}} = \arccos \frac{z_S - z_R}{d^{\text{SR}}}$  and  $\varphi^{\text{AoA}} = \arctan \frac{y_S - y_R}{x_S - x_R}$  at the RIS, the LoS paths associated with  $l = l_p = 0$  and  $p = 0$  are given by:

$$h_{n,m,0}^{\text{SR}_r} = \sqrt{\frac{K^{\text{SR}}}{K^{\text{SR}} + 1}} \omega_{MN}^{k_0^{\text{SR}_r}(nM+m)} \times [\mathbf{a}_{\text{UPA}}(\theta^{\text{AoA}}, \varphi^{\text{AoA}})]_r. \quad (9)$$

For the UPA having  $R_y$  and  $R_z$  elements on the  $y$  and  $z$  axes, the array response is given by:

$$\mathbf{a}_{\text{UPA}}(\theta, \varphi) = [1, \dots, \exp\{j \frac{2\pi}{\lambda} d [r_y \sin \theta \cos \varphi + r_z \sin \varphi]\}, \dots, \exp\{j \frac{2\pi}{\lambda} d [(R_y - 1) \sin \theta \cos \varphi + (R_z - 1) \sin \varphi]\}]^T, \quad (10)$$

where we have  $[1 \leq r_y \leq R_y]$ ,  $[1 \leq r_z \leq R_z]$  and  $(R = R_y R_z)$ , while  $(d = \frac{\lambda}{2})$  denotes the antenna spacing. Based on (9), the LoS fading gain  $\tilde{h}_0^{\text{SR}_r}$  of (8) associated with  $p = 0$  is now given by  $\tilde{h}_0^{\text{SR}_r} = \sqrt{\frac{K^{\text{SR}}}{K^{\text{SR}} + 1}} [\mathbf{a}_{\text{UPA}}(\theta^{\text{AoA}}, \varphi^{\text{AoA}})]_r$ . Moreover, the LoS Doppler index in (9) is given by  $k_0^{\text{SR}_r} = \lceil f_D^{\text{SR}} \cos(\phi_0^{\text{SR}_r}) NT \rceil$ , where the angle is  $(\phi_0^{\text{SR}_r} = \arctan \frac{y_S - y_R}{x_S - x_R})$ .

Following this, the signal received at the  $r$ -th RIS element is modelled in the TD and DD-domain as follows:

$$y_{n,m}^{\text{SR}_r} = \sum_{l=0}^{L^{\text{SR}}-1} h_{n,m,l}^{\text{SR}_r} s_{n,m-l} = \sum_{p=0}^{P^{\text{SR}}-1} \tilde{h}_p^{\text{SR}_r} \omega_{MN}^{k_p^{\text{SR}_r}(nM+m-l_p)} s_{n,m-l_p}, \quad (11)$$

where we have  $\mathfrak{b}(k_p^{\text{SR}_r}, l_p) = 1$  for all the  $P^{\text{SR}}$  resolvable paths.

#### E. The RIS-Destination (RD) Link

The RD link has  $P^{\text{RD}}$  resolvable paths associated with the maximum delay of  $\tau_{\text{max}}^{\text{RD}}$ . The NLoS model of the RD link  $h_{n,m,l}^{\text{RD}_r}$  is the same as (8) for the SR link, where the superscript of SR is replaced by RD. Furthermore, based on the azimuth and elevation AoDs of  $(\theta^{\text{AoD}} = \arccos \frac{z_D - z_R}{d^{\text{RD}}})$  and  $(\varphi^{\text{AoD}} = \arctan \frac{y_D - y_R}{x_D - x_R})$ , the LoS model of the RD link is formulated as:

$$h_{n,m,0}^{\text{RD}_r} = \sqrt{\frac{K^{\text{RD}}}{K^{\text{RD}} + 1}} \omega_{MN}^{k_0^{\text{RD}_r}(nM+m)} \times [\mathbf{a}_{\text{UPA}}(\theta^{\text{AoD}}, \varphi^{\text{AoD}})]_r. \quad (12)$$

The LoS fading gain is given by  $\tilde{h}_0^{\text{RD}_r} = \sqrt{\frac{K^{\text{RD}}}{K^{\text{RD}} + 1}} [\mathbf{a}_{\text{UPA}}(\theta^{\text{AoD}}, \varphi^{\text{AoD}})]_r$ , while the LoS Doppler index is given by  $k_0^{\text{RD}_r} = \lceil f_D^{\text{RD}} \cos(\phi_0^{\text{RD}_r}) NT \rceil$ . Furthermore, upon applying the time-varying RIS phase rotations, the

signal received at the destination from the  $r$ -th RIS element is expressed as:

$$\begin{aligned} y_{n,m}^{\text{RD}_r} &= \sum_{l=0}^{L^{\text{RD}}-1} h_{n,m,l}^{\text{RD}_r} \alpha_{n,m-l}^r y_{n,m-l}^{\text{SR}_r} \\ &= \sum_{p=0}^{P^{\text{RD}}-1} \tilde{h}_p^{\text{RD}_r} \omega_{MN}^{k_p^{\text{RD}_r} (nM+m-l_p)} \alpha_{n,m-l_p}^r y_{n,m-l_p}^{\text{SR}_r}, \end{aligned} \quad (13)$$

where we have  $\mathfrak{b}(k_p^{\text{RD}_r}, l_p) = 1$  for all the  $P^{\text{RD}}$  resolvable paths.

### F. Received Signal Modelling

Based on (7), (11) and (13), the received TD signal is formulated as:

$$\begin{aligned} y_{n,m} &= \sum_{l_0=0}^{L^{\text{SD}}-1} h_{n,m,l_0}^{\text{SD}} s_{n,m-l_0} + v_{n,m} \\ &+ \sum_{r=1}^R \sum_{l_1=0}^{L^{\text{SR}}-1} \sum_{l_2=0}^{L^{\text{RD}}-1} \alpha_{n,m-l_2}^r h_{n,m-l_2,l_1}^{\text{SR}_r} h_{n,m,l_2}^{\text{RD}_r} s_{n,m-l_1-l_2} \\ &= \sum_{l=0}^{L-1} h_{n,m,l} s_{n,m-l} + v_{n,m}, \end{aligned} \quad (14)$$

where  $v_{n,m}$  refers to the AWGN associated with a zero mean and a variance of  $N_0$ . The total number of TDL taps is  $L = \max(L^{\text{SD}}, L^{\text{SR-RD}})$ , where the RIS-reflected links impose an increased number of multipaths associated with  $L^{\text{SR-RD}} = L^{\text{SR}} + L^{\text{RD}} - 1$ . The equivalent TD fading that models the composite direct and RIS-reflected fading channels is given by:

$$h_{n,m,l} = \begin{cases} h_{n,m,l}^{\text{SD}} + \sum_{r=1}^R h_{n,m,l}^{\text{SR-RD}_r}, & 0 \leq l \leq \min(L^{\text{SD}}-1, L^{\text{SR-RD}}-1), \\ h_{n,m,l}^{\text{SD}}, & L^{\text{SR-RD}} \leq l \leq L-1, \text{ if } L = L^{\text{SD}}, \\ \sum_{r=1}^R h_{n,m,l}^{\text{SR-RD}_r}, & L^{\text{SD}} \leq l \leq L-1, \text{ if } L = L^{\text{SR-RD}}. \end{cases} \quad (15)$$

where the cascaded RIS-reflected fading is:

$$h_{n,m,l}^{\text{SR-RD}_r} = \sum_{\forall l_1+l_2=l} \alpha_{n,m-l_2}^r h_{n,m-l_2,l_1}^{\text{SR}_r} h_{n,m,l_2}^{\text{RD}_r}. \quad (16)$$

Similarly, the received DD-domain signal is expressed as:

$$\begin{aligned} y_{n,m} &= \sum_{p_0=0}^{P^{\text{SD}}-1} \tilde{h}_{p_0}^{\text{SD}} \omega_{MN}^{k_{p_0}^{\text{SD}} (nM+m-l_{p_0})} s_{n,m-l_{p_0}} \\ &+ \sum_{r=1}^R \sum_{p_1=0}^{P^{\text{SR}}-1} \sum_{p_2=0}^{P^{\text{RD}}-1} \alpha_{n,m-l_{p_2}}^r \tilde{h}_{p_1}^{\text{SR}_r} \tilde{h}_{p_2}^{\text{RD}_r} \\ &\quad \times \omega_{MN}^{k_{p_2}^{\text{RD}_r} l_{p_1}} \omega_{MN}^{(k_{p_1}^{\text{SR}_r} + k_{p_2}^{\text{RD}_r}) (nM+m-l_{p_1}-l_{p_2})} s_{n,m-l_{p_1}-l_{p_2}} + v_{n,m}. \end{aligned} \quad (17)$$

It is of vital importance to transform the time-varying RIS phase rotations  $\alpha_{n,m}^r$  to the corresponding DD-domain representation, which will be presented in the next section.

## III. OPTIMIZATION OF RIS REFLECTION COEFFICIENTS

### A. RIS Configuration in the TF-Domain

The time-varying RIS phase rotations are strictly non-frequency-selective [48], [51], [58], where the same set of RIS phase rotations will be applied to all  $M$  SCs or equivalently to  $L$  TDL taps. Therefore, the RIS optimization problem may be formulated in the TD and FD as:

$$\begin{aligned} \max_{\{\alpha_{n,m}^r\}_{r=1}^R} & \sum_{l=0}^{L-1} |h_{n,m,l}|^2 = \max_{\{\alpha_{n,m}^r\}_{r=1}^R} \sum_{m=0}^{M-1} |\bar{h}_{n,m}|^2, \\ \text{subject to} & |\alpha_{n,m}^r| = 1, \forall r = 1, \dots, R. \end{aligned} \quad (18)$$

The CFRs  $\bar{h}_{n,m}$  of (18) are obtained by the FFT of the CIRs  $h_{n,m,l}$  of (15), which will be further elaborated on in Sec IV. This problem is non-convex due to the constant modulus constraint, which can only be suboptimally solved by the successive convex approximation (SCA) technique in the FD [48]. The SCA obtains a stationary point at the cost of polynomial complexity in terms of  $M$  and  $R$ . Furthermore,

the RIS configuration based on (18) requires instantaneous CSI knowledge of both the LoS and NLoS paths fed back through the control link, which is impractical in time-varying SAGIN applications. As a remedy, we seek the RIS reflection coefficients that maximize the dominant LoS tap as seen in [48], [58], which is shown to have negligible performance difference with respect to the SCA algorithm. In summary, the low-complexity RIS configuration based on statistical CSI is formulated by:

$$\begin{aligned} \max_{\{\alpha_{n,m}^r\}_{r=1}^R} & |h_{n,m,0}|^2, \\ \text{subject to} & |\alpha_{n,m}^r| = 1, \forall r = 1, \dots, R, \end{aligned} \quad (19)$$

where the LoS of (15) is given by:

$$h_{n,m,0} = h_{n,m,0}^{\text{SD}} + \sum_{r=1}^R \alpha_{n,m}^r h_{n,m,0}^{\text{SR}_r} h_{n,m,0}^{\text{RD}_r}. \quad (20)$$

Based on this, the RIS configuration in the TD is given by [48], [58]:

$$\alpha_{n,m}^r = \frac{h_{n,m,0}^{\text{SD}} \left( h_{n,m,0}^{\text{SR}_r} h_{n,m,0}^{\text{RD}_r} \right)^*}{\left| h_{n,m,0}^{\text{SD}} \left( h_{n,m,0}^{\text{SR}_r} h_{n,m,0}^{\text{RD}_r} \right)^* \right|}. \quad (21)$$

### B. RIS Configuration in the DD-Domain

For the time-varying frequency-selective fading model, the general rule for transforming the TD representation to the DD-domain representation is  $h_{n,m,l} \rightarrow \tilde{h}_p \omega_{MN}^{k(nM+m-l)}$ , where we have the time-invariant  $\tilde{h}_p$ , Doppler index  $k$  and delay index  $l$ . Similarly, for the time-varying non-frequency-selective RIS phase rotations, we propose the following TD to DD-domain transformation:

$$\alpha_{n,m}^r = \tilde{\alpha}^r \omega_{MN}^{k^{\text{RIS}_r} (nM+m)}, \quad (22)$$

which is associated with a time-invariant phase  $\tilde{\alpha}^r$  and a virtual Doppler index  $k^{\text{RIS}_r}$ . We note that the RIS itself does not suffer from the Doppler effect, hence the nominal ‘‘virtual’’ Doppler index. Moreover, the RIS is non-frequency-selective, i.e. it cannot be tuned for different TDL taps, hence we have no delay index. Based on (22), the RIS can now tune the phase and Doppler differences between the SD link and the RIS-reflected links in the DD-domain. In other words, the time-varying RIS configuration is simplified to setting the two time-invariant parameters of  $\tilde{\alpha}^r$  and  $k^{\text{RIS}_r}$ .

Therefore, the RIS-reflected link of (16) may be represented in the DD-domain as:

$$\begin{aligned} h_{n,m,l}^{\text{SR-RD}_r} &= \sum_{\forall l_{p_1}+l_{p_2}=l} \tilde{\alpha}^r \tilde{h}_{p_1}^{\text{SR}_r} \tilde{h}_{p_2}^{\text{RD}_r} \\ &\quad \times \omega_{MN}^{(k_{p_2}^{\text{RD}_r} + k^{\text{RIS}_r}) l_{p_1}} \omega_{MN}^{(k_{p_1}^{\text{SR}_r} + k_{p_2}^{\text{RD}_r} + k^{\text{RIS}_r}) (nM+m-l_{p_1}-l_{p_2})}. \end{aligned} \quad (23)$$

This facilitates the simplified DD-domain representation of the received signal model of (17):

$$y_{n,m} = \sum_{p=0}^{P-1} \tilde{h}_p \omega_{MN}^{k_p(nM+m-l_p)} s_{n,m-l_p} + v_{n,m}, \quad (24)$$

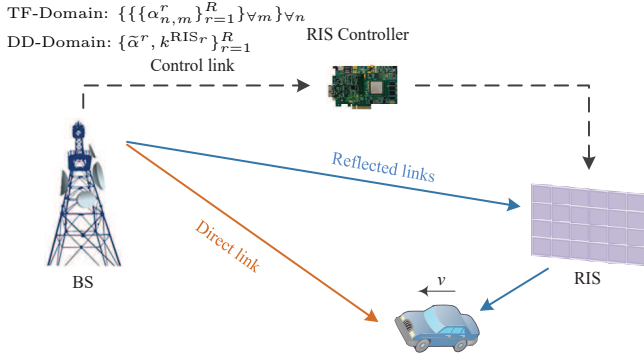


Fig. 2: Schematic illustration of the RIS configuration in the TF and DD domains in RIS assisted vehicular communication systems.

where the composite direct and RIS-reflected DD-domain fading channels are expressed as:

$$\begin{aligned} \tilde{h}_p &= \tilde{h}_p^{\text{SD}} \mathbf{b}(k_p^{\text{SD}}, l_p) \\ &+ \sum_{r=1}^R \sum_{\forall l_{p_1} + l_{p_2} = l_p} \tilde{\alpha}^r \tilde{h}_{p_1}^{\text{SR}_r} \tilde{h}_{p_2}^{\text{RD}_r} \omega_{MN}^{(k_{p_2}^{\text{RD}_r} + k^{\text{RIS}_r})l_{p_1}} \\ &\quad \times \mathbf{b}(k_{p_1}^{\text{SR}_r}, l_{p_1}) \mathbf{b}(k_{p_2}^{\text{RD}_r}, l_{p_2}), \end{aligned} \quad (25)$$

while the Doppler index and delay index are given by:

$$\begin{aligned} k_p &= \begin{cases} k_p^{\text{SD}}, & \mathbf{b}(k_p^{\text{SD}}, l_p) = 1, \\ k_{p_1}^{\text{SR}_r} + k_{p_2}^{\text{RD}_r} + k^{\text{RIS}_r}, & \mathbf{b}(k_{p_1}^{\text{SR}_r}, l_{p_1}) \mathbf{b}(k_{p_2}^{\text{RD}_r}, l_{p_2}) = 1. \end{cases} \\ l_p &= \begin{cases} l_p^{\text{SD}}, & \mathbf{b}(k_p^{\text{SD}}, l_p) = 1, \\ l_{p_1} + l_{p_2}, & \mathbf{b}(k_{p_1}^{\text{SR}_r}, l_{p_1}) \mathbf{b}(k_{p_2}^{\text{RD}_r}, l_{p_2}) = 1. \end{cases} \end{aligned} \quad (26)$$

Finally, based on the discussions in Sec. III-A, the low-complexity RIS configuration of (21) based on statistical CSI in the TD may be transformed to the DD-domain as follows:

$$k^{\text{RIS}_r} = k_0^{\text{SD}} - k_0^{\text{SR}_r} - k_0^{\text{RD}_r}, \quad \tilde{\alpha}^r = \angle \tilde{h}_0^{\text{SD}} - \angle \tilde{h}_0^{\text{SR}_r} \tilde{h}_0^{\text{RD}_r}, \quad (27)$$

where the LoS Doppler indices and the time-invariant gains are defined in (6), (9) and (12).

### C. Comparison between RIS configurations in the TF and DD domains

The schematic illustration of the RIS configuration is portrayed by Fig. 2 for a vehicular communication system. The control information on RIS configuration can be conveyed by a separate link, such as Bluetooth, and the associated time duration has negligible impact on the data rate compared to the pilot overhead, as assumed in [48]–[52]. As portrayed by Fig. 2, the TF-domain RIS configuration based on (21) requires instantaneous feedback on the time-varying RIS phase rotations  $\{\{\{\alpha_{n,m}^r\}_{r=1}^R\}_{\forall m}\}_{\forall n}$  based on the time-varying fading channels  $\{\{h_{n,m,0}^{\text{SD}}\}_{\forall m}\}_{\forall n}$ ,  $\{\{\{h_{n,m,0}^{\text{SR}_r}\}_{r=1}^R\}_{\forall m}\}_{\forall n}$  and  $\{\{\{h_{n,m,0}^{\text{RD}_r}\}_{r=1}^R\}_{\forall m}\}_{\forall n}$ . By contrast, the DD-domain RIS configuration based on (22) only requires the pair of time-invariant DD-domain parameters of  $\{\tilde{\alpha}^r, k^{\text{RIS}_r}\}_{r=1}^R$  optimized by (27), which substantially reduced the feedback complexity and overhead.

It is worth noting that the RIS configurations of (21) and (27) in the TF and DD domains rely purely on the LoS paths, which are assumed to be known by the BS, as assumed in [25], [41]–[44], [80]–[83]. The statistical CSI of LoS paths include

positioning-related path loss, AoA/AoD as well as the vehicular velocity, which can be obtained by the global positioning system (GPS) that is essential for SAGIN applications. As a result, channel estimation for RIS configuration at the RIS is avoided, but full CSI estimation for both LoS and NLoS is still needed for the composite direct and RIS-reflected links for the sake of signal detection at the destination node, which will be detailed in Sec. IV.

### D. The Number of Paths is Increased by RISs

The deployment of RIS naturally increases the number of paths. Explicitly, in the TD, the set of resolvable TDL delays is given by:

$$\{l_0\}_{\forall l_0 \in [0, L^{\text{SD}} - 1]} \cup \{l_1 + l_2\}_{\forall l_1 \in [0, L^{\text{SR}} - 1], \forall l_2 \in [0, L^{\text{RD}} - 1]}, \quad (28)$$

where  $\cup$  refers to the union of two sets. As discussed in Sec. II-F, the RIS-reflected links generate an increased number of paths associated with an increased range for the delay index  $l \in [0, L - 1]$ , where the maximum delay of the RIS-assisted system is given by  $L = \max(L^{\text{SD}}, L^{\text{SR}} + L^{\text{RD}} - 1)$ .

Furthermore, in the DD-domain, the set of resolvable paths is represented by:

$$\begin{aligned} &\{(k_{p_0}^{\text{SD}}, l_{p_0})\}_{\forall p_0 \in [0, P^{\text{SD}} - 1]} \\ &\cup \{(k_{p_1}^{\text{SR}_r} + k_{p_2}^{\text{RD}_r} + k^{\text{RIS}_r}, l_{p_1} + l_{p_2})\}_{\forall p_1 \in [0, P^{\text{SR}} - 1], \forall p_2 \in [0, P^{\text{RD}} - 1]}, \end{aligned} \quad (29)$$

which substantially increases both the Doppler index range and the delay index range. The Doppler index range becomes  $[-k_{\max}, k_{\max}]$ , where the maximum Doppler index is given by  $k_{\max} = k_{\max}^{\text{SR}} + k_{\max}^{\text{RD}} + k_{\max}^{\text{RIS}}$ , while the maximum RIS Doppler index of (27) is given by  $k_{\max}^{\text{RIS}} = k_{\max}^{\text{SD}} + k_{\max}^{\text{SR}} + k_{\max}^{\text{RD}}$ . The maximum Doppler indices for the SD, SR and RD links are defined in Secs. II-C, II-D and II-E, respectively. The delay index range is given by  $l \in [0, L - 1]$  as seen in TD. Therefore, the total number of resolvable paths in the DD-domain may be expressed as  $P^{\text{SD}} \leq L^{\text{SD}}(2k_{\max}^{\text{SD}} + 1)$  without RIS and  $P^{\text{SD}} \leq L(2k_{\max} + 1)$  with RIS.

In order to demonstrate this, Fig. 3 portrays the numbers of resolvable paths in the TD and DD-domain for a RIS-assisted high speed train communications system (Scenario Train in Fig. 1) versus the maximum delay  $\tau_{\max}$  and RIS size in the 5G FR1 S-band (2.6GHz) and FR2 K-band (26GHz). More explicitly, Fig. 3(a) and Fig. 3(b) demonstrate that the RIS increased the number of paths in the TD from the range of  $[0, L^{\text{SD}} - 1]$  without RIS to  $[0, L - 1]$  with RIS, which is substantially lower than the increase in the DD-domain from  $P^{\text{SD}} \leq L^{\text{SD}}(2k_{\max}^{\text{SD}} + 1)$  without RIS to  $P^{\text{SD}} \leq L(2k_{\max} + 1)$  with RIS. Fig. 3(c) and Fig. 3(d) further demonstrate that owing to the fact that the non-frequency-selective RIS phase rotations do not impose extra delay for increasing  $R$ , the number of paths has only been substantially increased in the DD-domain for both the S-band associated with  $P^i = 2L^i$  and K-band having  $P^i = 0.6L^i$ .

## IV. OTFS WAVEFORMS AND CHANNEL ESTIMATION

Based on the TF- and DD-domains representation of RIS channel modelling of Sec. II and the RIS configuration of



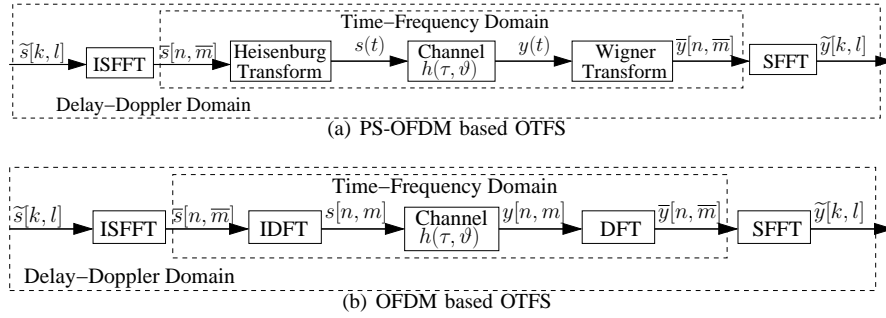


Fig. 4: The schematics of OTFS based on pulse-shaped OFDM (PS-OFDM) using bi-thogonal pulses [64], [70], [77] and OTFS based on OFDM using rectangular pulses [67], [74], [77].

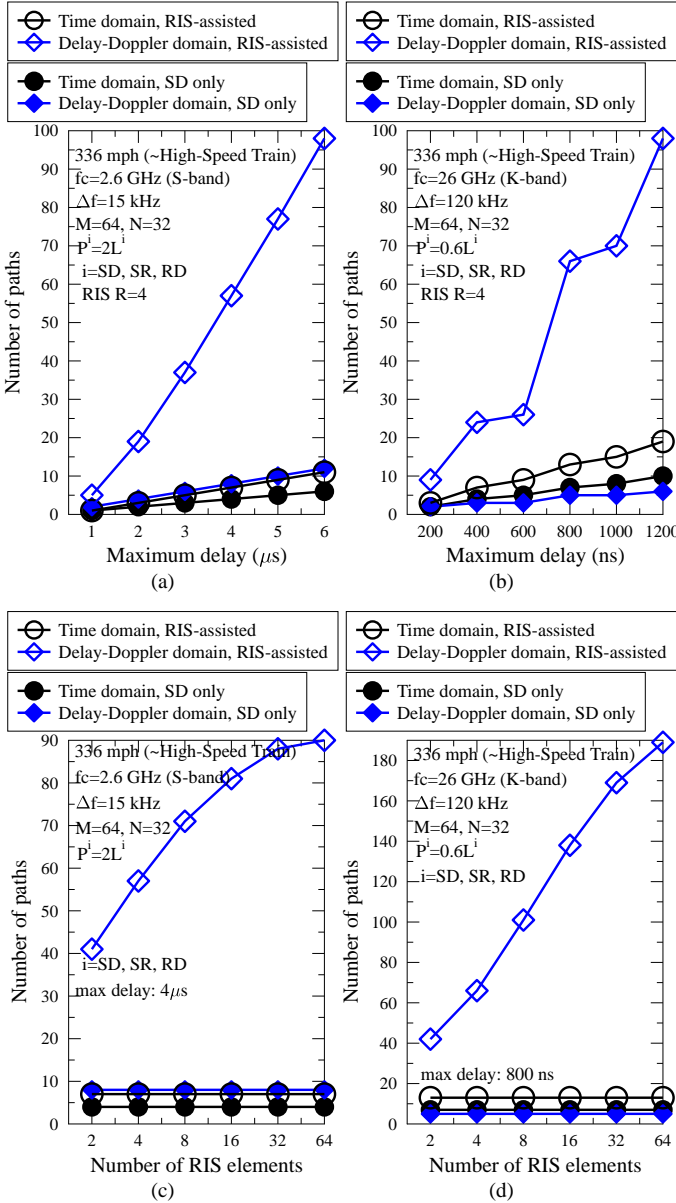


Fig. 3: The numbers of path in the TD and DD-domain for the RIS-assisted train system (Scenario Train in Fig. 1) with respect to maximum delay  $\tau_{\max}$  and RIS size at 5G FR1 S-band (2.6GHz) and FR2 K-band (26GHz).

Sec. III, the OTFS waveforms and channel estimation techniques are introduced in this section. The schematics of OTFS based on pulse-shaped OFDM (PS-OFDM) using bi-thogonal pulses [64], [70], [77] and OTFS based on OFDM using rectangular pulses [67], [74], [77] are portrayed by Fig. 4, which are detailed in Sec. IV-A and Sec. IV-B, respectively. The channel estimation techniques conducted in the FD, TD and DD-domain are conceived for OFDM and OTFS in Sec. IV-D, which are compatible with 4G/5G OFDM infrastructure.

#### A. OTFS Based on Pulse-Shaped OFDM

The schematic of PS-OFDM based OTFS [64], [70], [77] is shown in Fig. 4(a), which is equivalent to ISFFT precoded PS-OFDM spanning over  $M$  SCs and  $N$  OFDM symbol durations. First of all, the OTFS transmitter modulates a total number of  $NM$  PSK/QAM symbols in the DD-domain as  $\{\{\tilde{s}[k, l]\}_{k=0}^{N-1}\}_{l=0}^{M-1}$ . The ISFFT is performed at the transmitter as:

$$\bar{s}[n, \bar{m}] = \frac{1}{\sqrt{NM}} \sum_{k=0}^{N-1} \sum_{l=0}^{M-1} \tilde{s}[k, l] \omega_N^{nk} \omega_M^{-\bar{m}l}. \quad (30)$$

Following this, the continuous-time Heisenberg transform is invoked at the transmitter as:

$$s(t) = \frac{1}{\sqrt{M}} \sum_{n=0}^{N-1} \sum_{\bar{m}=0}^{M-1} \bar{s}[n, \bar{m}] g_{tx}(t - nT) \times e^{j2\pi\bar{m}\Delta f(t-nT)} \Big|_{t=\frac{n(M+M_{cp})+m}{M}T \approx nT + \frac{m}{M}T}, \quad (31)$$

where  $M_{cp}$  is the length of the cyclic prefix (CP), while  $g_{tx}(t)$  refers to the transmit PS filter. Under the condition that  $M_{cp} \ll M$ , (31) may be expressed in discrete-time as:

$$s[n, m] = \frac{1}{\sqrt{M}} \sum_{\bar{m}=0}^{M-1} \bar{s}[n, \bar{m}] g_{tx}\left(\frac{m}{M}T\right) \omega_M^{\bar{m}m} = s'[n, m] g_{tx}\left(\frac{m}{M}T\right). \quad (32)$$

where we have  $s'[n, m] = \frac{1}{\sqrt{M}} \sum_{\bar{m}=0}^{M-1} \bar{s}[n, \bar{m}] \omega_M^{\bar{m}m} = \frac{1}{\sqrt{N}} \sum_{k=0}^{N-1} \tilde{s}[k, m] \omega_N^{nk}$ . The received signal of (1) spanning over  $N$  OFDM symbol durations is extended as:

$$y(t) = \int \int \sum_{p=0}^{P-1} \tilde{h}_p \delta(\tau - \tau_p) \delta(\vartheta - \vartheta_p) s(t - \tau) \times e^{j2\pi\vartheta(t-\tau)} d\tau d\vartheta \Big|_{t=\frac{nM+m}{M}T, \tau=\frac{l}{M\Delta f}, \vartheta=\frac{k}{NT}}, \quad (33)$$

which may be expressed in discrete-time as<sup>1</sup>:

$$y[n, m] = \sum_{p=0}^{P-1} \tilde{h}_p \omega_{MN}^{k_p[nM+m-l_p]} s[n, \langle m-l_p \rangle_M] + v[n, m], \quad (34)$$

where the composite direct and RIS-reflected links in the DD-domain are expressed in the same way as in (24). The OTFS receiver invokes the Wigner transform formulated as:

$$\bar{y}(t, f) = \int g_{rx}^*(t' - t) y(t') e^{-j2\pi f(t' - t)} dt' \Big|_{t=nT, f=\bar{m}\Delta f}, \quad (35)$$

where  $g_{rx}(t)$  refers to the receiver PS filter. The continuous-time representation of (35) may be expressed in discrete-time as:

$$\begin{aligned} \bar{y}[n, \bar{m}] &= \frac{1}{\sqrt{M}} \sum_{n'=0}^{N-1} \sum_{m'=0}^{M-1} g_{rx}^* \left( (n-n')T + \frac{m'}{M}T \right) y[n', m'] \\ &\quad \times \omega_M^{-\bar{m}[(n'-n)M+m']} \\ &= \frac{1}{\sqrt{M}} \sum_{n'=0}^{N-1} \sum_{m'=0}^{M-1} \sum_{p=0}^{P-1} g_{rx}^* \left( (n'-n)T + \frac{m'}{M}T \right) \tilde{h}_p \\ &\quad \times s[n', \langle m' - l_p \rangle_M] \omega_{MN}^{k_p[nM+m'-l_p]} \omega_M^{-\bar{m}[(n'-n)M+m']} + \bar{v}[n, \bar{m}]. \end{aligned} \quad (36)$$

Let us assume that the ideal transmitter and receiver PS filters have the following cross-ambiguity function exhibiting the bi-orthogonal property:

$$\begin{aligned} A_{r_x, t_x} &= \int g_{rx}^*(t' - t) g_{tx}(t') e^{-j2\pi f(t' - t)} dt' \Big|_{t=nT + \frac{m}{M}T, \\ &\quad t' = n'T + \frac{m'}{M}T, \\ &\quad f = \bar{m}\Delta f + \frac{k}{NT}} \\ &= \delta[n] \delta[m] \text{ for } k \in [\min_p k_p, \max_p k_p] \text{ and } l \in [\min_p l_p, \max_p l_p]. \end{aligned} \quad (37)$$

Then the Wigner transform of (36) may be extended as (38), where we have  $y'[n, m] = \sum_{p=0}^{P-1} \tilde{h}_p \omega_{MN}^{k_p[nM+m-l_p]} s'[n, \langle m'-l_p \rangle_M] + v[n, m]$ . Finally, the SFFT at the receiver leads to the following input-output relationship for the OTFS waveform expressed by (39), where  $\tilde{s}[\langle k - k_p \rangle_N, \langle l - l_p \rangle_M]$  and  $\tilde{y}[k, l]$  refer to the modulated symbols and the received symbols both in the DD-domain. The AWGN term in the DD-domain  $\tilde{v}[k, m] = \frac{1}{\sqrt{N}} \sum_{n=0}^{N-1} v[n, m] \omega_N^{-nk}$  has the same distribution characteristics as the TD AWGN in (24).

### B. OTFS Based on OFDM

The ideal bi-orthogonal waveform of (37) is not always realistic in practice. Therefore, the OFDM-based OTFS concept based on practical rectangular waveforms is proposed in [67], [74], [77], which is portrayed in Fig. 4(b). More explicitly, following the ISSFT of (30), the transmitter performs IDFT as:

$$s[n, m] = \frac{1}{\sqrt{M}} \sum_{\bar{m}=0}^{M-1} \bar{s}[n, \bar{m}] \omega_M^{m\bar{m}} = \frac{1}{\sqrt{N}} \sum_{k=0}^{N-1} \tilde{s}[k, m] \omega_N^{nk}. \quad (40)$$

Upon obtaining the received signal of (34), the receiver performs DFT formulated as:

$$\begin{aligned} \bar{y}[n, \bar{m}] &= \frac{1}{\sqrt{M}} \sum_{m=0}^{M-1} y[n, m] \omega_M^{-m\bar{m}} \\ &= \frac{1}{\sqrt{M}} \sum_{m=0}^{M-1} \sum_{p=0}^{P-1} \tilde{h}_p s[n, \langle m - l_p \rangle_M] \omega_{MN}^{k_p[nM+m-l_p]} \omega_M^{-m\bar{m}} \end{aligned} \quad (41)$$

<sup>1</sup>We note that with a slight abuse of notation,  $y_{n,m}$ ,  $s_{n,m}$  and  $v_{n,m}$  of (17) in TD are represented as  $y[n, m]$ ,  $s[n, m]$  and  $v[n, m]$  in line with the OTFS representations in this section.

Finally, the SFFT at the receiver leads to the following input-output relationship of (42).

We note that (42) is derived under the assumptions that the CP length is small  $M_{cp} \ll M$  and a CP is inserted for each OFDM duration for the sake of compatibility with the existing OFDM infrastructure. If a single CP is added to the entire OTFS frame, the TD circular convolution of (34) becomes MN-periodic according to:

$$y[n, m] = \sum_{p=0}^{P-1} \tilde{h}_p \omega_{MN}^{k_p[nM+m-l_p]} s[\langle nM+m-l \rangle_{MN}] + v[n, m]. \quad (43)$$

As a result, the input-output relationship of (42) becomes:

$$\tilde{y}[k, l] = \sum_{p=0}^{P-1} \tilde{h}_p \tilde{T}(k, l, k_p, l_p) \tilde{s}[\langle k - k_p \rangle_N, \langle l - l_p \rangle_M] + \tilde{v}[k, l], \quad (44)$$

where the DD indices based phase rotations are defined as:

$$\tilde{T}(k, l, k_p, l_p) = \begin{cases} \omega_{MN}^{k_p \langle l - l_p \rangle_M} & l \geq l_p \\ \omega_N^{-(k - k_p)} \omega_{MN}^{k_p \langle l - l_p \rangle_M} = \omega_N^{-k} \omega_{MN}^{k_p \langle l - l_p \rangle_M} & l < l_p \end{cases} \quad (45)$$

### C. OFDM and OTFS in Matrix Form

The input-output relationship of the OTFS waveforms of (39), (42) and (44) may all be expressed in the following matrix form:

$$\tilde{\mathbf{y}} = \tilde{\mathbf{H}} \tilde{\mathbf{s}} + \tilde{\mathbf{v}}. \quad (46)$$

The  $\kappa$ -th element in  $\tilde{\mathbf{y}} \in \mathcal{C}^{MN \times 1}$  is given by  $\tilde{y}_\kappa = \tilde{y}[k, l]$ , where we have  $k = \lfloor \frac{\kappa}{M} \rfloor$  and  $l = \kappa - kM$ . Similarly, the  $\kappa$ -th elements in  $\tilde{\mathbf{s}} \in \mathcal{C}^{MN \times 1}$  and  $\tilde{\mathbf{v}} \in \mathcal{C}^{MN \times 1}$  are given by  $\tilde{s}_\kappa = \tilde{s}[k, l]$  and  $\tilde{v}_\kappa = \tilde{v}[k, l]$ , respectively. The DD-domain fading matrix  $\tilde{\mathbf{H}} \in \mathcal{C}^{MN \times MN}$  is time-invariant and sparse, where the non-zero elements are given by  $\tilde{\mathbf{H}}_{\kappa, \iota} = \tilde{h}_p \omega_{MN}^{-k_p l_p}$  associated with  $\iota = M \times \langle k - k_p \rangle_N + \langle l - l_p \rangle_M$  for OTFS based on PS-OFDM of (39). Similarly, we have  $\tilde{\mathbf{H}}_{\kappa, \iota} = \tilde{h}_p \omega_{MN}^{k_p \langle l - l_p \rangle_M}$  and  $\tilde{\mathbf{H}}_{\kappa, \iota} = \tilde{h}_p \tilde{T}(k, l, k_p, l_p)$  for OTFS based on OFDM using the symbol CP of (42) and frame CP of (44), respectively.

Based on (46), the MMSE detector [75], [76] may be formulated as  $\tilde{\mathbf{z}} = (\tilde{\mathbf{H}}^H \tilde{\mathbf{H}} + N_0 \mathbf{I}_{MN})^{-1} \tilde{\mathbf{H}}^H \tilde{\mathbf{y}}$ . Furthermore, based on exploiting the sparsity of  $\tilde{\mathbf{H}}$ , a range of MP detectors are conceived in [77]–[79]. Similarly, for the OFDM regime, a total number of  $NM$  PSK/QAM symbols are modulated in the TF-domain as  $\{\{\tilde{s}[n, m]\}_{n=0}^{N-1}\}_{m=0}^{M-1}$ , and the TD received signal model of (34) may be expressed in matrix form as:

$$\mathbf{y} = \mathbf{H} \mathbf{s} + \mathbf{v}, \quad (47)$$

where  $\mathbf{H}$  is modelled based on TD fading  $h_{n,m,l} = \sum_{p=0}^{P-1} \tilde{h}_p \omega_{MN}^{k_p(nM+m-l_p)} \mathbf{b}(k_p, l_p)|_{l=l_p}$ . In the face of double-selectivity, the TD fading matrix  $\mathbf{H}$  is no longer circulant, and hence the MMSE detection may be performed in the TD as  $\mathbf{z} = (\mathbf{H}^H \mathbf{H} + N_0 \mathbf{I}_M)^{-1} \mathbf{H}^H \mathbf{y}$ . The MP detectors can also be conceived based on the sparsity of  $\mathbf{H}$  following the same philosophy of [77]–[79], where there are  $L$  non-zero CIR taps on each row and column of  $\mathbf{H}$ . Considering that the number of resolvable paths  $P$  is substantially increased by deploying RISs, we invoke the MMSE detector for both the OFDM and OTFS systems for the sake of fair comparison.

$$\begin{aligned} \bar{y}(t, f) &= \frac{1}{\sqrt{M}} \sum_{n'=0}^{N-1} \sum_{m'=0}^{M-1} \sum_{p=0}^{P-1} g_{rx}^* \left( (n'-n)T + \frac{m'}{M}T \right) g_{tx} \left( \frac{\langle m'-l_p \rangle M T}{M} \right) \omega_{MN}^{-j(\bar{m}'-\bar{m})N-k_p[(n'-n)M+m']} \\ &\quad \times \tilde{h}_p s' [n', \langle m'-l_p \rangle M] \omega_{MN}^{j(\bar{m}'-\bar{m})N-k_p[(n'-n)M+m']} \omega_{MN}^{k_p[nM+m'-l_p]} \omega_M^{-\bar{m}[(n'-n)M+m']} + \tilde{v}[n, \bar{m}] |_{n=n', \bar{m}=\bar{m}'} \end{aligned} \quad (38)$$

$$\begin{aligned} &= \frac{1}{\sqrt{M}} \sum_{m'=0}^{M-1} \sum_{p=0}^{P-1} \tilde{h}_p s' [n, \langle m'-l_p \rangle M] \omega_{MN}^{k_p(nM-l_p)} \omega_M^{-\bar{m}m'} + \tilde{v}[n, \bar{m}] = \frac{1}{M} \sum_{m=0}^{M-1} y'[n, m] \omega_M^{-\bar{m}m}, \\ \tilde{y}[k, l] &= \frac{1}{\sqrt{MN}} \sum_{n=0}^{N-1} \sum_{\bar{m}=0}^{M-1} \bar{y}[n, \bar{m}] \omega_N^{-nk} \omega_M^{\bar{m}l} = \sum_{p=0}^{P-1} \tilde{h}_p \omega_{MN}^{-k_p l_p} \tilde{s}[\langle k-k_p \rangle_N, \langle l-l_p \rangle_M] + \tilde{v}[k, l], \end{aligned} \quad (39)$$

$$\tilde{y}[k, l] = \frac{1}{\sqrt{MN}} \sum_{n=0}^{N-1} \sum_{\bar{m}=0}^{M-1} \bar{y}[n, \bar{m}] \omega_N^{-nk} \omega_M^{\bar{m}l} = \sum_{p=0}^{P-1} \tilde{h}_p \omega_{MN}^{k_p(l-l_p)} \tilde{s}[\langle k-k_p \rangle_N, \langle l-l_p \rangle_M] + \tilde{v}[k, l]. \quad (42)$$

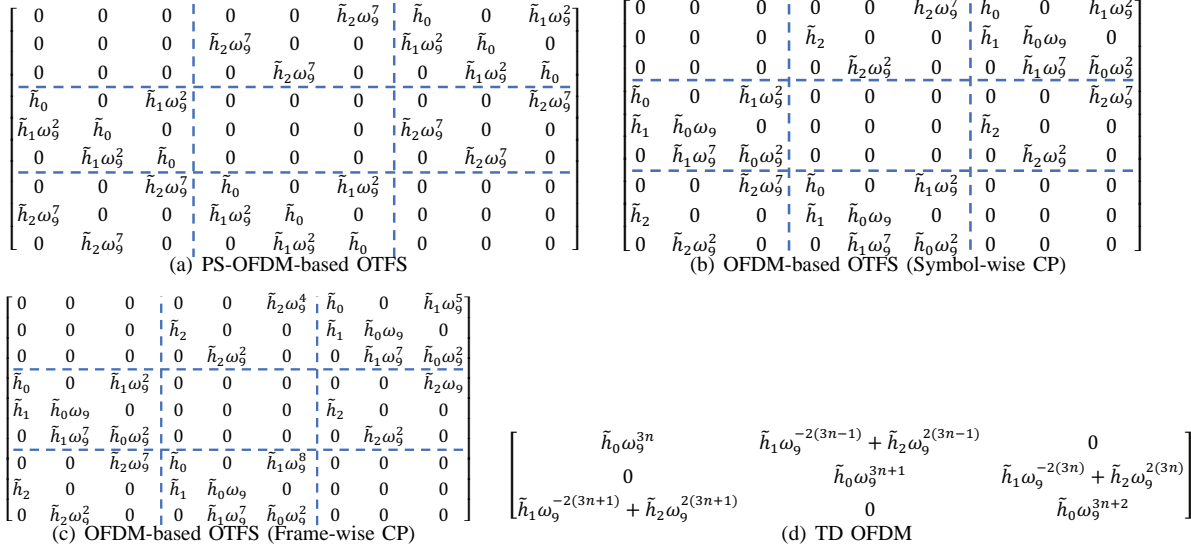


Fig. 5: Examples of the DD-domain fading matrix of (46) and the TD-domain fading matrix of (47), where we have  $N = 3$ ,  $M = 3$  and  $[k_p, l_p] = \{[1, 0], [-2, 1], [2, 1]\}$ .

In order to better understand the input-output representations, let us consider a simple example of an OTFS system having  $N = 3$  and  $M = 3$  operating at Ka-band  $f_c = 38.5 \leq \frac{M}{L}$  GHz and using a SCS of  $\Delta f = 30$  kHz. The vehicle speed is assumed to be 540 km/h and hence the associated maximum Doppler frequency is given by  $\nu_{\max} = 19.25$  kHz. The fading has  $P = 3$  resolvable paths associated with indices of  $[k_p, l_p] = \{[1, 0], [-2, 1], [2, 1]\}$ . As a result, the DD-domain fading matrices for PS-OFDM-based OTFS, OFDM-based OTFS with symbol/frame-wise CP are presented in Figs. 5(a), (b) and (c), respectively, while the TD-domain fading matrix for OFDM is shown in Fig. 5(d). It can be readily seen in Fig. 5 that the DD-domain fading matrix  $\tilde{\mathbf{H}}$  is time-invariant and sparse, where there are  $P$  non-zero elements on each row and each column. Furthermore, the fading matrix  $\tilde{\mathbf{H}}$  in Fig. 5(a) has a favourable block-wise circulant structure, where the non-zero fading taps associated with the same index  $p$  are shifted in position on each row, but are associated with the same phase rotation. However, for the fading matrix  $\tilde{\mathbf{H}}$  in Figs. 5(b) and (c), the phase rotations of the non-zero fading taps on each row are determined by their specific delay and Doppler indices. This will impose extra requirements for the channel estimation techniques discussed in the next section.

#### D. Channel Estimation for OFDM and OTFS

A suite of FD and TD interpolation-based channel estimation techniques were conceived in our previous work [58] for RIS using OFDM in doubly-selective fading, which are characterized in Figs. 6(a) and (b), respectively. More explicitly, the pilot spacing in the FD requires  $\mathcal{N}_{PS}^{FD} \leq \frac{M}{L}$ , so that at least

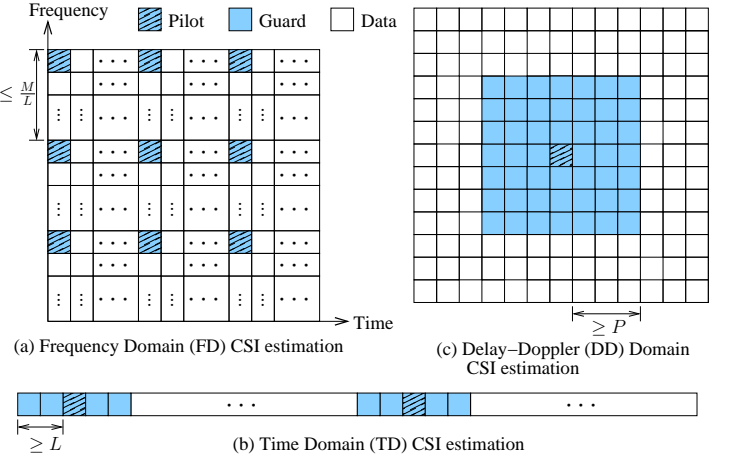


Fig. 6: Schematic illustration of FD, TD and DD-domain channel estimation techniques.

$\mathcal{N}_p^{FD} = \frac{M}{\mathcal{N}_{PS}^{FD}} \geq L$  pilots are inserted at the SC indices of  $\bar{m}' \in \{0, \mathcal{N}_{PS}^{FD}, 2\mathcal{N}_{PS}^{FD}, \dots, (\mathcal{N}_p^{FD} - 1)\mathcal{N}_{PS}^{FD}\}$ . The first step of the FD channel estimation technique of Fig. 6(a) follows a “horizontal comb”, where the MMSE interpolation is performed based on  $N_w$  pilot observations that are associated with the OFDM symbol indices  $n' \in \{n - \lfloor \frac{N_w-1}{2} \rfloor \mathcal{N}_{PS}^{TD}, \dots, n - \mathcal{N}_{PS}^{TD}, n, n + \mathcal{N}_{PS}^{TD}, \dots, n + (N_w - 1 - \lfloor \frac{N_w-1}{2} \rfloor) \mathcal{N}_{PS}^{TD}\}$ . The estimated FD CFR at the  $\bar{m}'$ -th subcarrier of the  $n$ -th OFDM symbol is given by:

$$\hat{h}_{n, \bar{m}'} = (\mathbf{w}_{n, \bar{m}'}^{\text{FD}})^H \hat{\mathbf{y}}_{n, \bar{m}'}^{\text{FD}} = \mathbf{e}_{n, \bar{m}'}^{\text{FD}} (\mathbf{C}_{n, \bar{m}'}^{\text{FD}})^{-1} \hat{\mathbf{y}}_{n, \bar{m}'}^{\text{FD}}, \quad (48)$$

where the MMSE filter’s input vector  $\hat{\mathbf{y}}_{n, \bar{m}'}^{\text{FD}} \in \mathcal{C}^{N_w \times 1}$  stores the  $N_w$  pilot observations, while the MMSE filter’s weights

are given by  $(\mathbf{w}_{n,\bar{m}'}^{\text{FD}})^H = \mathbf{e}_{n,\bar{m}'}^{\text{FD}} (\mathbf{C}_{n,\bar{m}'}^{\text{FD}})^{-1}$ . Owing to the time-varying nature of the TF-domain fading, the elements in  $\mathbf{e}_{n,\bar{m}'}^{\text{FD}} \in \mathcal{C}^{1 \times N_w}$  and  $\mathbf{C}_{n,\bar{m}'}^{\text{FD}} \in \mathcal{C}^{N_w \times N_w}$  are evaluated by the correlation functions as  $[\mathbf{e}_{n,\bar{m}'}^{\text{FD}}]_p = \Upsilon^{\text{FD}}(n - n_p, \bar{m}' - \bar{m}_{p_1})$ ,  $[\mathbf{C}_{n,\bar{m}'}^{\text{FD}}]_{p_1,p_2} = \Upsilon^{\text{FD}}(n_{p_1} - n_{p_2}, \bar{m}_{p_1} - \bar{m}_{p_2})$  for  $p_1 \neq p_2$  and  $[\mathbf{C}_{n,\bar{m}'}^{\text{FD}}]_{p,p} = \Upsilon^{\text{FD}}(0,0) + N_0$ , where the RIS fading correlation function  $\Upsilon^{\text{FD}}(\cdot)$  is modelled in [58]. Following the ‘‘horizontal comb’’ interpolation of (48), the ‘‘vertical comb’’ interpolation is performed for the  $n$ -th OFDM symbol as follows. The  $L$  TDL taps are obtained by performing  $\mathcal{N}_p^{\text{FD}}$ -point IDFT on the  $\mathcal{N}_p^{\text{FD}}$  estimated  $\{\hat{h}_{n,\bar{m}'}\}_{\forall \bar{m}'}$  of (48), and then the full FD fading estimation is obtained by performing  $M$ -point DFT on the  $L$  TDL taps. In summary, the MSE of the FD MMSE filter of (48) is given by  $\sigma_{\text{MSE}}^2 = 1 - \mathbf{e}_{n,\bar{m}'}^{\text{FD}} (\mathbf{C}_{n,\bar{m}'}^{\text{FD}})^{-1} (\mathbf{e}_{n,\bar{m}'}^{\text{FD}})^H$ .

The above FD interpolation method still relies on the subcarrier orthogonality for the ‘‘vertical comb’’ operation, which may suffer from error floor as the Doppler frequency is substantially increased in SAGINs. In order to mitigate this problem, the TD interpolation-based channel estimation technique of Fig. 6(b) directly inserts a dirac delta impulse-based CP in the TD as:

$$s_{0,m} = \begin{cases} \rho_p^{\text{TD}}, & m = 0 \\ 0, & m = \pm 1, \pm 2, \dots, \pm \mathcal{N}_{\text{guard}}^{\text{TD}} \end{cases}, \quad (49)$$

where the power of the pilot impulse  $\rho_p^{\text{TD}}$  aims for ensuring that the transmission power obeys  $\sum_{\forall m} |s_{0,m}|^2 = 2\mathcal{N}_{\text{cp}}^{\text{TD}} + 1$ , while the zeros in (49) are referred to as guard intervals in Fig. 6(b). Following the TD convolution between the impulse-based pilot CP and the TDL taps, the CIRs are estimated one by one without interference, under the condition of  $\mathcal{N}_{\text{guard}}^{\text{TD}} \geq L$ . Following this, MMSE-based interpolation is performed in the TD in order to obtain the estimated TD CIR for the  $m$ -th data-carrying sample of the  $n$ -th OFDM symbol as follows:

$$\hat{h}_{n,m,l} = (\mathbf{w}_{n,m,l}^{\text{TD}})^H \tilde{\mathbf{y}}_{n,l}^{\text{TD}} = \mathbf{e}_{n,m,l}^{\text{TD}} (\mathbf{C}_{n,m,l}^{\text{TD}})^{-1} \tilde{\mathbf{y}}_{n,l}^{\text{TD}}, \quad (50)$$

where the MMSE filter’s input vector  $\tilde{\mathbf{y}}_{n,l}^{\text{TD}} \in \mathcal{C}^{N_w \times 1}$  stores the  $N_w$  pilot observations on the  $l$ -th TDL tap from  $N_w$  CPs of the  $N_w$  neighbouring OFDM symbols, while the MMSE filter’s weights are given by  $(\mathbf{w}_{n,m,l}^{\text{TD}})^H = \mathbf{e}_{n,m,l}^{\text{TD}} (\mathbf{C}_{n,m,l}^{\text{TD}})^{-1}$ . The elements in  $\mathbf{e}_{n,m,l}^{\text{TD}} \in \mathcal{C}^{1 \times N_w}$  and  $\mathbf{C}_{n,m,l}^{\text{TD}} \in \mathcal{C}^{N_w \times N_w}$  are evaluated by the TD correlation functions as  $[\mathbf{e}_{n,m,l}^{\text{TD}}]_p = \Upsilon_l^{\text{TD}}((n - n_p)M + m_p)$ ,  $[\mathbf{C}_{n,m,l}^{\text{TD}}]_{p_1,p_2} = \Upsilon_l^{\text{TD}}((n_{p_1} - n_{p_2})M + m_{p_1} - m_{p_2})$  for  $p_1 \neq p_2$  and  $[\mathbf{C}_{n,m,l}^{\text{TD}}]_{p,p} = \Upsilon_l^{\text{TD}}(0) + N_0$ . The detailed evaluations on the TD correlation functions  $\Upsilon_l^{\text{TD}}(\cdot)$  can be found in [58]. Similarly, the MSE of the TD MMSE filter of (50) is given by  $\sigma_{\text{MSE}}^2 = 1 - \mathbf{e}_{n,m,l}^{\text{TD}} (\mathbf{C}_{n,m,l}^{\text{TD}})^{-1} (\mathbf{e}_{n,m,l}^{\text{TD}})^H$ .

In stark contrast to the time-varying TF-domain fading, the DD-domain fading is time-invariant, which no longer needs the high-complexity interpolation operations. More explicitly, the DD-domain channel estimation technique is portrayed in Fig. 6(c), where a dirac delta impulse is transmitted in the DD-domain based on (46) as:

$$\tilde{\mathbf{s}}_{\kappa} = \begin{cases} \rho_p^{\text{DD}}, & \kappa = \kappa_p \\ 0, & \kappa = \kappa_p \pm 1, \kappa_p \pm 2, \dots, \kappa_p \pm \mathcal{N}_{\text{guard}}^{\text{DD}} \\ \tilde{s}[k, l], & \text{otherwise} \end{cases}, \quad (51)$$

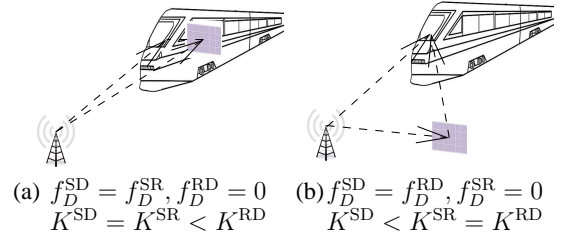


Fig. 7: Schematic illustration of two mobility scenarios exemplified by train: (a) RIS is attached onto the vehicle; (b) RIS is stationary.

where the power of the pilot impulse  $\rho_p^{\text{DD}}$  aims for maintaining the constant OTFS frame power of  $MN$ . The guard interval has to obey  $\mathcal{N}_{\text{guard}}^{\text{DD}} \geq P$ . Thanks to the guard interval, based on (46), the  $\kappa_p$ -th column of  $\tilde{\mathbf{H}}$  is estimated by the pilot impulse without interference by:

$$\tilde{\mathbf{h}}_{\kappa,\kappa_p} = \tilde{\mathbf{y}}_{\kappa} / \tilde{s}_{\kappa_p}. \quad (52)$$

The complete fading matrix  $\tilde{\mathbf{H}}$  may be recovered based on the input-output relationship of the OTFS waveforms of (39), (42) and (44). The number of paths  $P$  may be estimated based on a detection threshold of  $\mathcal{T}$ , where the signals received within the guard interval that are associated with a higher power than  $\mathcal{T}$  are considered to be non-zero elements. In summary, the associated MSE of the single-tap equalization is simply given by:

$$\sigma_{\text{MSE}}^2 = E(|\tilde{\mathbf{h}}_{\kappa,\kappa_p} - \hat{\mathbf{h}}_{\kappa,\kappa_p}|) = N_0 / \rho_p^{\text{DD}}. \quad (53)$$

## V. PERFORMANCE RESULTS

### A. Simulation Scenarios and Parameters

The RIS assisted SAGIN scenarios and parameters shown in Fig. 1 are considered in this paper. For the sake of fair comparison, we adopt  $M = 64$  and  $N = 32$  for both OFDM and OTFS, where the 5G system’s scalable numerology of  $\text{SCS} = 2^\mu \times 15$  kHz associated with non-negative integers  $\mu$  is invoked [5], [10]–[12]. The simulations are conducted in the licensed 5G NR bands, namely the UHF-band (0.8GHz), L-band (1.5GHz), S-band (2.6GHz) and C-band (4.7GHz) of FR1 as well as K-band (26GHz) and Ka-band (28.5GHz) of FR2. The resolvable paths are assumed to be more sparse in FR2 than in FR1. For the channel estimation techniques, the parameters of the FD and TD schemes seen in Figs. 6(a) and (b) can be found in [58]. For the DD-domain channel estimation, an entire OTFS frame is dedicated to estimating the substantially increased number of paths in the RIS system. In this way, both OFDM and OTFS are supported, and the estimation threshold is set to  $\mathcal{T} = \frac{3}{N_0}$ .

Furthermore, the mobility scenarios of RIS are exemplified by train communication in Fig. 7, where the RIS is either attached to the vehicle or being stationary on the ground. Moreover, the PL parameters that pertain to distances, antenna gain and PLE are exemplified in Table V. More explicitly, first of all, the BS coordinate is set to be  $(x_S, y_S, z_S) = (0, 0, 0)$  and the user coordinate is initialized for different scenarios as summarized in Table V. The RIS is assumed to be deployed at 1 meter away from the user, i.e. we have  $x_R = x_D - 1$ ,  $y_R = y_D$  and  $z_R = z_D$ . Secondly, the achievable antenna gain is given by  $G_e = \frac{4\pi A_e}{\lambda^2}$ , where the antenna apertures at the

TABLE V: Summary of path loss parameters initialized for the SAGIN scenarios of Fig. 1.

Scenarios	User $(x_D, y_D, z_D)$	BS aperture $A_e^{BS}$	User aperture $A_e^{user}$	SD PLE $\gamma^{SD}$
Car	(300, 1, 1)	80 cm <sup>2</sup>	40 cm <sup>2</sup>	3.64
Train	(500, -2, 1)	80 cm <sup>2</sup>	40 cm <sup>2</sup>	3.51
Airplane	(200, 100, 10000)	16 dm <sup>2</sup>	1.6 dm <sup>2</sup>	3.02
Supersonic UAV	(2000, 1000, 20000)	16 dm <sup>2</sup>	1.6 dm <sup>2</sup>	2.95
Hypersonic UAV	(20000, 10000, 20000)	16 dm <sup>2</sup>	1.6 dm <sup>2</sup>	2.91
Low Earth Orbit	(100000, 10000, 2000000)	60 cm radius	60 cm radius	2.65

BS and user are exemplified for different SAGIN scenarios in Table V. Thirdly, the PLE of the RIS-reflected link is assumed to be  $\gamma^{SRD} = 2.0$ , while the PLEs of the direct SD link are exemplified for different SAGIN scenarios in Table V. We note that the PL parameters are fixed to the specific values summarized by Table V at first so that we can investigate the effects of all other factors, including channel estimation, Ricean  $K$  factor, delay and Doppler in Sec. V-B, Sec. V-C, Sec. V-D and Sec. V-E. The effect of varying the PL parameters will be further investigated in Sec. V-F.

### B. RIS Channel Estimation Results

Fig. 8 investigates the effect of vehicular speed on channel estimation, where the train scenario of Fig. 1 is considered, while the mobility scenario of Fig. 7(a) is assumed. *First of all*, Figs. 8(a)-(c) demonstrate that substantial performance improvements are achieved by using RIS with as few as  $R = 4$  independent reflecting elements. *Secondly*, Fig. 8(a) shows that the FD channel estimation technique suffers from error floors at 200 mph, which is further deteriorated at 400 mph and 600 mph as seen in Fig. 8(b) and Fig. 8(c), respectively. This is expected indeed, because the FD channel estimation of Fig. 6(a) relies on SC orthogonality, which is corrupted by the increased Doppler frequency. *Thirdly*, the TD channel estimation technique is shown to perform well at 200 mph in Fig. 8(b), but error floors start to emerge at 400 mph and 600 mph, as seen in Fig. 8(b) and Fig. 8(c), respectively. This is due to the fact that the MMSE-based TD interpolation requires lower pilot spacing at higher Doppler frequencies, which can no longer be satisfied when the pilot spacing is reduced to the minimum of the size of a single OFDM symbol. *Finally*, it is strongly evidenced by Figs. 8(a)-(c) that the DD-domain channel estimation is capable of providing reliable performance at different vehicular speeds. This is due to the fact that the fading representations in the DD-domain are time-invariant, which no longer requires any interpolation, as long as the intrinsic system characteristics remain unchanged.

In order to further justify our motivations, Fig. 9 portrays the performance of the channel estimation methods that are designed primarily for stationary scenarios, which include using LoS only, using the DFT pattern of [50]–[52] and using the ON/OFF pattern of [48], [49]. It can be seen in Fig. 9 that in the face of doubly-selective fading, the TF-domain channel estimation methods without interpolation all suffer from error floors even at a modest vehicle speed of 200 mph. By contrast, the TD and FD interpolation-based channel estimation techniques as well as the proposed DD-domain channel estimation method summarized in Sec. IV-D exhibit improved performance results, as evidenced by Fig. 9.

The effect of the SCS  $\Delta f$  is investigated in Fig. 10 in the context of RIS-assisted supersonic UAV systems (Scenario

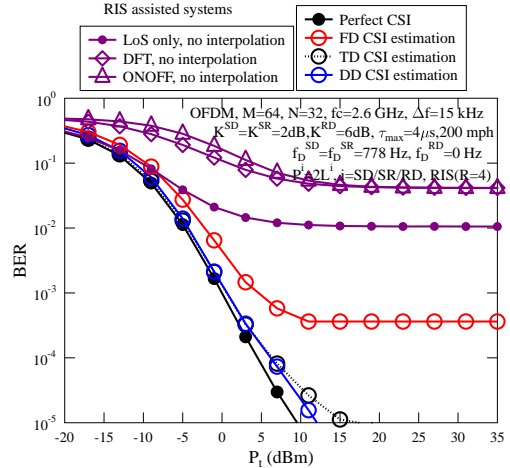


Fig. 9: Effect of TF-domain interpolation: BER results of RIS-assisted train system (Scenario Train in Fig. 1) using OFDM, where the TF-domain channel estimation methods without interpolation including using LoS only, using DFT pattern [50]–[52] and using ON/OFF pattern [48], [49] are compared to the methods presented in Fig. 8(a).

Supersonic UAV in Fig. 1), where the DD-domain channel estimation technique is invoked for the OTFS waveforms. *First of all*, Fig. 10(a) demonstrates that given the maximum Doppler frequency of 8894Hz, the SCS of  $\Delta f = 15$ kHz is sufficient for all OTFS waveforms in the absence of both RIS and channel estimation. *Secondly*, Fig. 10(b) demonstrates that an increased  $\Delta f = 30$ kHz is required for supporting the RIS system, due to the fact that the deployment of RIS extends the Doppler index range, as discussed in Sec. III-D. *Thirdly*, Fig. 10(c) demonstrates that for realistic DD-domain channel estimation, the SCS of  $\Delta f = 15$ kHz is no longer sufficient for the OTFS waveforms based on OFDM. This is due to the fact that the effective range of Doppler frequencies is given by  $[-f_D^{SD}, f_D^{SD}]$ , which leads to ambiguities for Doppler index localization, when we have  $f_D^{SD} > \frac{1}{2}\Delta f$ . Nonetheless, Fig. 10(c) also evidences that the OTFS based on PS-OFDM using the idealistic bi-orthogonal waveform is not affected, thanks to the favourable block-wise circulant structure of its fading matrix  $\tilde{\mathbf{H}}$ , as discussed in Sec. IV-C. *Therefore*, *fourthly*, the increased SCS of  $\Delta f = 30$ kHz is required for effective channel estimation on the direct SD link, as seen in Fig. 10(d). Furthermore, *finally*, the higher SCS of  $\Delta f = 60$ kHz is required for supporting high-quality RIS channel estimation, as seen in Fig. 10(e).

### C. Normalized MSE and Complexity Comparison

Fig. 11 portrays the normalized MSE and complexity comparison between the FD, TD and DD-domain channel estimation techniques for a RIS-assisted high-speed train system. First of all, Fig. 11(a) demonstrates that the FD technique that still relies on the subcarrier orthogonality suffers from the

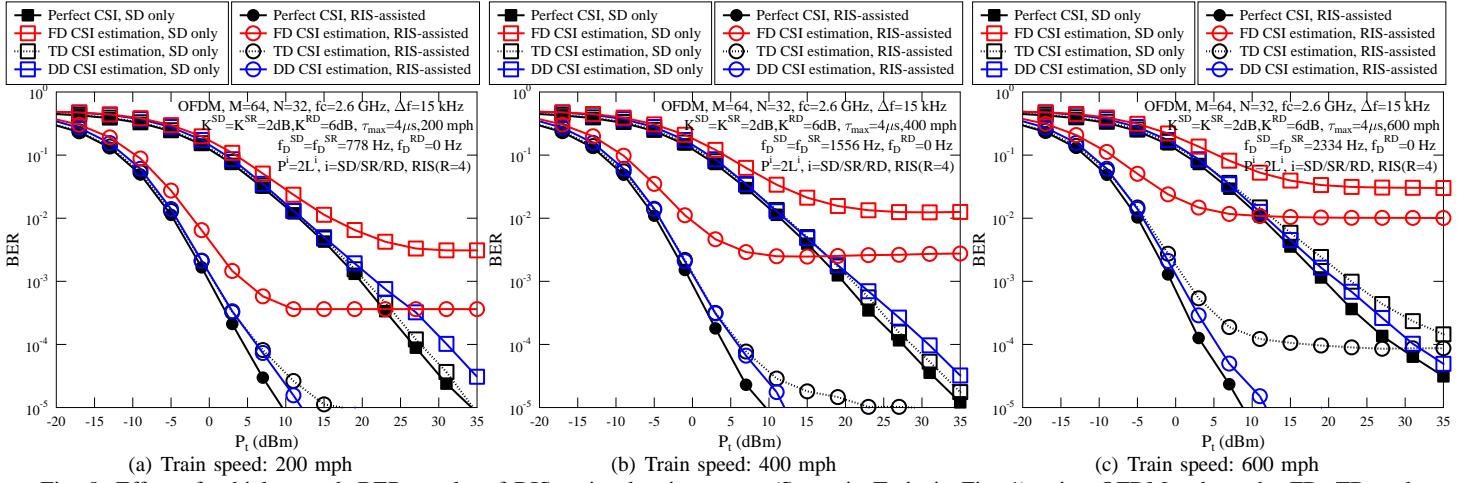


Fig. 8: Effect of vehicle speed: BER results of RIS-assisted train system (Scenario Train in Fig. 1) using OFDM, where the FD, TD and DD-domain channel estimation techniques are invoked.

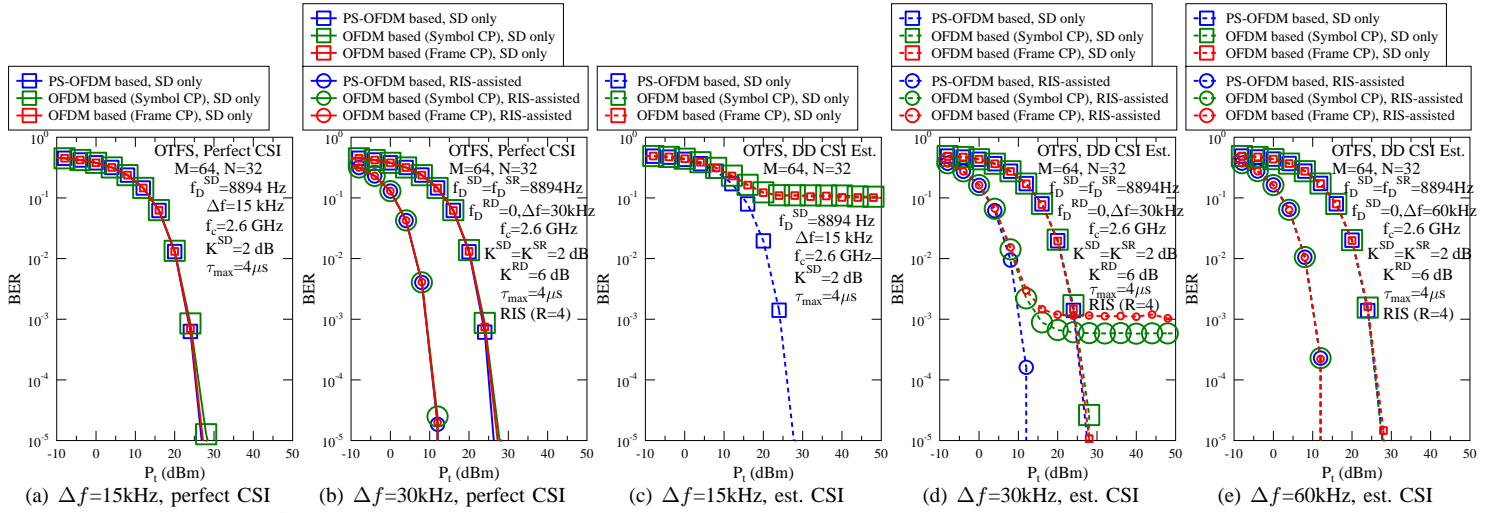


Fig. 10: Effect of SCS  $\Delta f$ : BER results of RIS-assisted supersonic UAV system (Scenario Supersonic UAV in Fig. 1) using OTFS, where the DD-domain channel estimation technique is invoked for the OTFS waveforms based on PS-OFDM and OFDM (with symbol CP and frame CP).

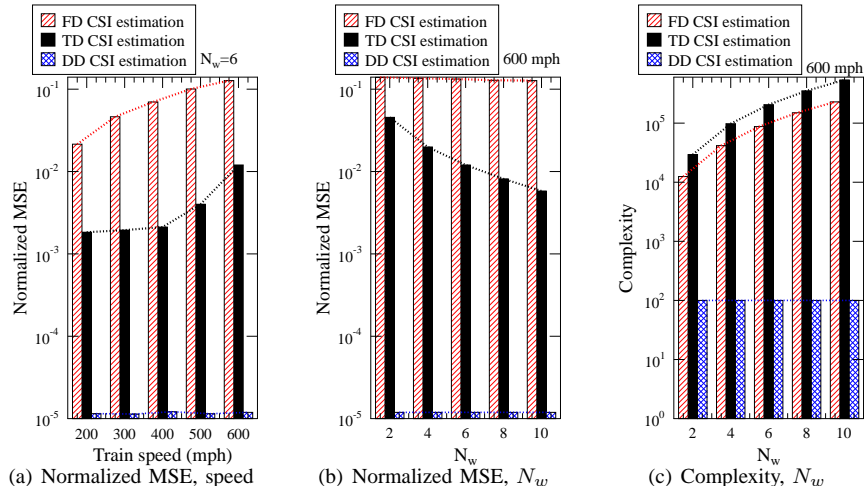


Fig. 11: Normalized MSE and complexity comparison between the FD, TD and DD-domain channel estimation techniques for RIS-assisted train system (Scenario Train in Fig. 1) using OFDM.

highest normalized MSE, followed by the TD interpolation-based technique, while the proposed DD-domain channel estimation method achieves the lowest normalized MSE, thanks to the time-invariant fading characteristics in the DD-domain. Secondly, Fig. 11(b) demonstrates that increasing the TF-domain interpolation window leads to an improved performance especially for the TD technique, where the performance of the FD technique is still predominantly eroded by the ICI, while the proposed DD-domain channel estimation method retains the lowest normalized MSE without interpolation. Finally, the complexities of the FD, TD and DD-domain channel estimation techniques are compared in Fig. 11(c) in terms of the numbers of real-valued multiplications, where the FD/TD correlation functions  $\Upsilon_l^{\text{FD}}(\cdot)$  and  $\Upsilon_l^{\text{TD}}(\cdot)$  defined in [58] are also taken into account. As expected, the FD and TD channel estimation techniques exhibit high complexities that grow with the interpolation window size  $N_w$ , while the proposed DD-domain channel estimation technique exhibits the lowest complexity, thanks to the elimination of the TF-domain interpolation.

#### D. RIS Assisted SAGIN Results

Fig. 12 summarizes the BER results of the RIS assisted SAGIN scenarios of Fig. 1 using OFDM and OTFS in the S-band (2.6GHz), where DD-domain channel estimation is invoked. For the sake of fair comparison, the OFDM-based OTFS waveform of Fig. 4(b) is invoked, where a single CP is inserted for each OFDM symbol duration. More explicitly, *first of all*, Figs. 12(a)-(f) demonstrate that the DD-domain channel estimation is effective for both OFDM and OTFS with or without RIS. *Secondly*, the RIS configuration of Sec. III based on statistical CSI is shown in Figs. 12(a)-(f) to achieve substantial performance advantages over both the scenario of using the direct SD link without RIS and the case of random RIS configuration for both OFDM and OTFS systems, where the random RIS configuration induces error floors due to the extended Doppler range. *Thirdly*, Figs. 12(a)-(f) evidence that OTFS systems outperform OFDM systems. It can also be observed that the OTFS assisted RIS systems achieve similar performance results in Figs. 12(a), (b), (d) and (e), which are associated with different vehicular speed but similar Ricean K factor, while the gap between OTFS and OFDM aided RIS systems is reduced in Figs. 12(c) and (f) due to their higher Ricean K factor. One may infer that as the Ricean K factor increases, the strong LoS dominates the signal propagation, which makes the difference between waveforms less relevant. This observation will be further investigated in terms of the effective throughput in the next section.

In summary, the results shown in Fig. 12 are extremely important for the operation of SAGIN systems, because in the worst-case scenarios of Fig. 1 the high mobility and the shadowing-induced deep fades may result in the vehicles travelling hundreds or even thousands of meters with a blocked control link. However, the combination of OTFS and RIS is capable of providing substantial performance improvements in all SAGIN scenarios, as seen in Fig. 12.

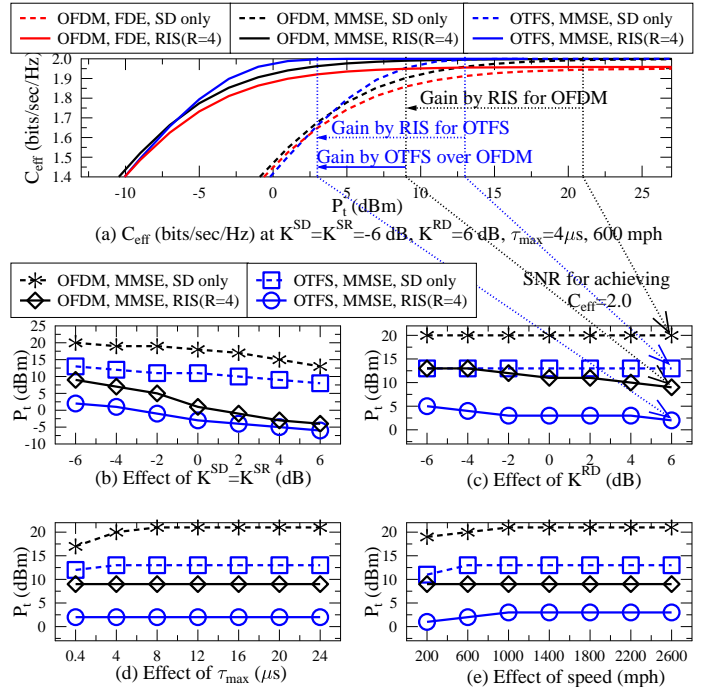


Fig. 13: Effective throughput of RIS assisted OTFS and OFDM systems with respect to fading parameters of Ricean K factor, maximum delay  $\tau_{\text{max}}$  and vehicle speed.

#### E. Effect Throughput Results

Fig. 13 investigates the effective throughputs of the RIS assisted OTFS and OFDM systems with respect to different fading parameters, where the train scenario of Fig. 1 is considered, while the mobility scenario of Fig. 7(a) is assumed. Based on the OTFS input-output relationship of (46), the effective throughput  $C_{\text{eff}}$  is evaluated by [13], [87], [93] (54), where the total number of combinations for  $\tilde{s}$  is given by  $\mathcal{I}$ , and the conditional probability based on (46) is formulated as  $p(\tilde{y}|\tilde{s}^t) = \frac{1}{\pi N_0} \exp(-\frac{\|\tilde{y} - \tilde{H}\tilde{s}^t\|^2}{N_0})$ . When QPSK constellation is used, the maximum  $C_{\text{eff}}$  of (54) is given by 2 bits/sec/Hz as seen in Fig. 13. The system throughput is given by  $C_{\text{eff}}M\Delta f$  bits/sec.

Fig. 13(a) confirms that the single-tap frequency-domain equalizer (FDE) of OFDM suffers from a performance loss with or without RIS, rendering it unsuitable for high-mobility SAGIN systems. By contrast, Fig. 13(a) demonstrates that the deployment of RIS results in an effective throughput for both OFDM and OTFS, which approaches their maximum  $C_{\text{eff}}$  of 2 bits/sec/Hz at reduced SNRs, as marked by ‘‘Gain by RIS for OFDM’’ and ‘‘Gain by RIS for OTFS’’ in Fig. 13(a), respectively. Furthermore, the RIS-assisted OTFS system achieves the maximum  $C_{\text{eff}}$  of 2 bits/sec/Hz at a lower SNR than its RIS-assisted OFDM counterpart, which is marked as ‘‘Gain by OTFS over OFDM’’ in Fig. 13(a).

In Figs. 13(b)-(e), the SNRs required for OFDM and OTFS systems with or without RIS achieving maximum  $C_{\text{eff}}$  are compared for different fading parameters. It can be seen in all of the Figs. 13(b)-(e) that the deployment of RIS results in substantial performance improvements over the case of using only the direct SD link in both OFDM and OTFS systems, even for Ricean K factors as low as -6 dB. Furthermore, the OTFS systems always outperform their OFDM counterparts.

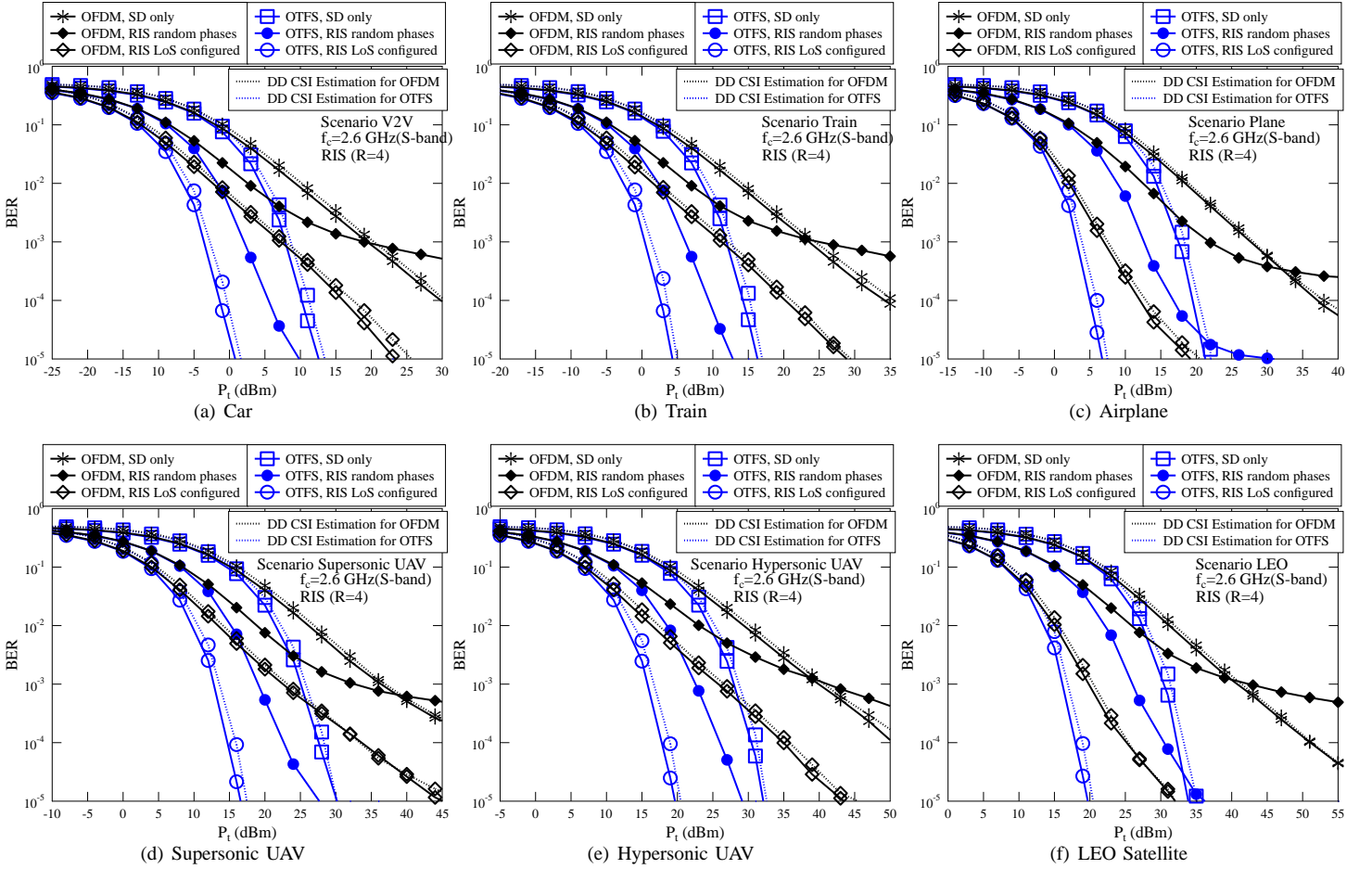


Fig. 12: Effect of RIS configuration for SAGIN: BER results of RIS-assisted SAGIN scenarios of Fig. 1 using OFDM and OTFS at S-band (2.6GHz), where DD-domain channel estimation is invoked. The RIS configuration of Sec. III is compared to random configuration.

$$\begin{aligned}
 C_{\text{eff}}(SNR) &= \max_{\{p(\tilde{s}^t)\}_{t=0}^{I-1}} \frac{1}{NM} \sum_{t=0}^{I-1} \int p(\tilde{\mathbf{y}}|\tilde{\mathbf{s}}^t) p(\tilde{\mathbf{s}}^t) \log_2 \frac{p(\tilde{\mathbf{y}}|\tilde{\mathbf{s}}^t)}{\sum_{t'=0}^{I-1} p(\tilde{\mathbf{y}}|\tilde{\mathbf{s}}^{t'}) p(\tilde{\mathbf{s}}^{t'})} d\tilde{\mathbf{y}} = \frac{1}{NM\mathcal{I}} \sum_{t=0}^{I-1} E \left[ \log_2 \frac{\mathcal{I} p(\tilde{\mathbf{y}}|\tilde{\mathbf{s}}^t)}{\sum_{t'=1}^{\mathcal{I}} p(\tilde{\mathbf{y}}|\tilde{\mathbf{s}}^{t'})} \right] \\
 &= \frac{1}{NM} \log_2 \mathcal{I} - \frac{1}{NM\mathcal{I}} \sum_{t=0}^{I-1} E \left\{ \log_2 \left[ \sum_{t'=0}^{I-1} \exp \left( \frac{-\|\tilde{\mathbf{H}}(\tilde{\mathbf{s}}^t - \tilde{\mathbf{s}}^{t'}) + \tilde{\mathbf{v}}\|^2 + \|\tilde{\mathbf{v}}\|^2}{N_0} \right) \right] \right\}.
 \end{aligned} \tag{54}$$

Additionally, Fig. 13(b) demonstrates that as  $K^{\text{SD}} = K^{\text{SR}}$  increases, the difference between the RIS-assisted OFDM system and RIS-assisted OTFS system becomes smaller, in line with our discussion in Sec. V-D. Nonetheless, the performance results of both RIS-assisted OFDM and RIS-assisted OTFS systems are stable for different  $K^{\text{RD}}$ ,  $\tau_{\text{max}}$  and vehicular speed values in Figs. 13(c), (d) and (e), respectively. This once again confirms that the RIS assisted OTFS systems are capable of providing superior performance compared to their OFDM counterparts in high-mobility strong-LoS SAGIN scenarios.

#### F. The Effects of Path Loss Parameters

In this section, we investigate the effects of PL parameters for the RIS-assisted train communication systems of Fig. 1, where the mobility scenario of Fig. 7(b) is assumed. The PLs of SD, SR and RD links are modelled by (4), where the coordinates are initialized as  $(x_S, y_S, z_S) = (0, 0, 0)$ ,  $(x_R, y_R, z_R) = (500, 4, 0)$  and  $(x_D, y_D, z_D) = (x_D, -2, 0)$ . The achievable antenna gain is  $G_e = \frac{4\pi A_e}{\lambda^2}$ , which is assumed to have an aperture of  $A_e^{\text{BS}} = 80\text{cm}^2$  at the BS and  $A_e^{\text{user}} = 40\text{cm}^2$  at the user.

Fig. 14(a) investigates the power-efficiency gain of using RIS, when the train user is travelling to different locations. The direct SD link suffers from obstacle-induced blockage and high NLoS attenuation with PLE of  $\gamma^{\text{SD}} = 3.8$ , while the RIS-reflected links are associated with  $\gamma^{\text{SR}} = \gamma^{\text{RD}} = 2.0$ . In Fig. 14(a), the transmit powers  $P_t$  (dBm) for  $\text{BER}=10^{-4}$  at different user location of  $(x_D, y_D, z_D) = (x_D, -2, 0)$  are recorded in the top right subfigure, while the power-efficiency gains are recorded in the bottom right subfigure. It is demonstrated by Fig. 14(a) that the RIS power-efficiency gain is maximized when the user is close to the location of RIS. On one hand, when the user moves closer to the BS, the direct SD link becomes strong enough without RIS, as evidenced by Fig. 14(a). On the other hand, when the user moves away from both the BS and the RIS, the RIS-reflected links begin to help more, especially as the RIS size  $R$  increases. However, the power-efficiency gain of the RIS gradually decreases, as  $x_D$  increases, which is due to the fact that the RIS-reflected links gradually become weaker, as evidenced by Fig. 14(a).

The effect of the PLE of the SD link  $\gamma^{\text{SD}}$  is investigated in Fig. 14(b), which demonstrates that the RIS is capable of achieving substantial power-efficiency improvements that



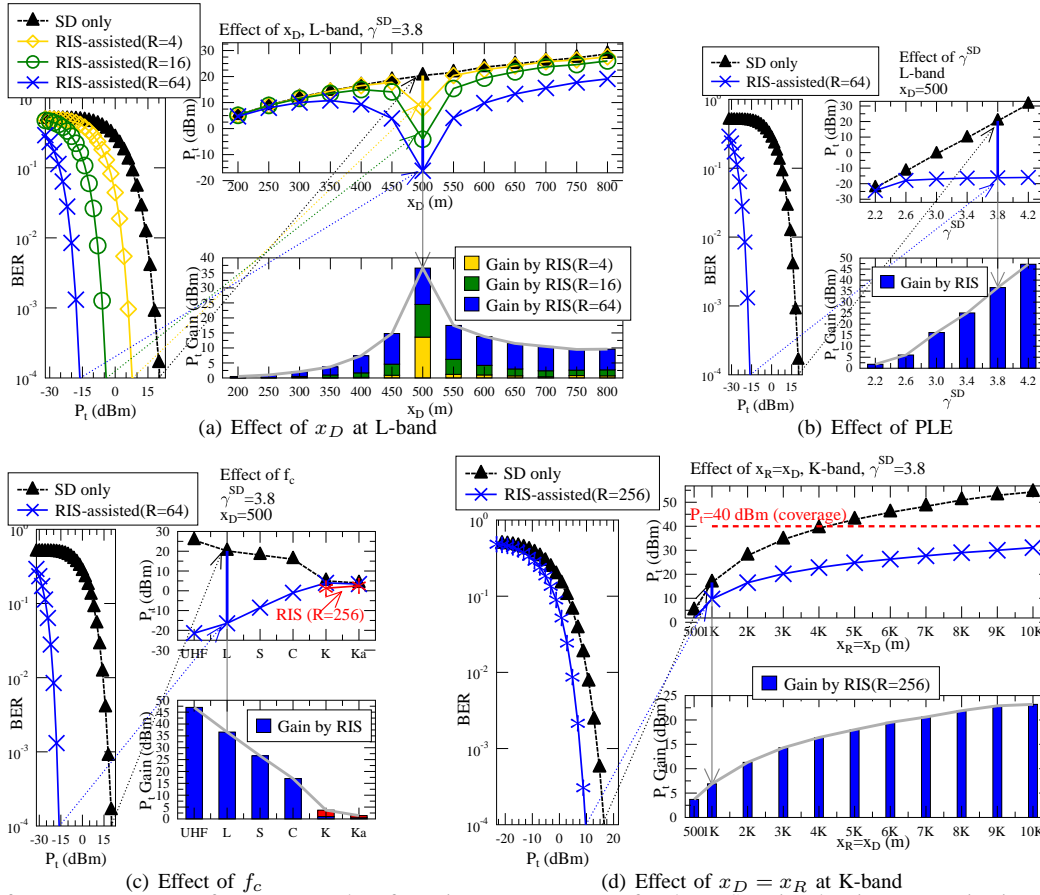


Fig. 14: Effect of PL parameters: Performance results of varying PL parameters for the RIS-assisted train communication systems of Fig. 1, where the mobility scenario of Fig. 7(b) is assumed.

increase with  $\gamma^{SD}$  for a wide range of  $\gamma^{SD} > 2.2$ . We note that in reality the PLE of the SD link may range from 2 to 6, depending on the blockage conditions [22].

Fig. 14(c) demonstrates that the RIS power-efficiency gain is reduced to a diminishing level even for a RIS size of  $R = 256$  in the higher FR2 K-band and Ka-band bands. This is due to the fact that the BS and user antenna apertures are fixed, which leads to higher antenna gain for the direct SD link, as  $f_c$  increases. Nonetheless, Fig. 14(d) further demonstrates that if the RIS is attached to the train, the deployment of RIS is capable of extending the coverage for the train over a long distance ranging up to 10 km in the K-band, where the SD link requiring more than 40 dBm is deemed to be out of coverage.

## VI. CONCLUSIONS

We proposed OTFS-based RIS-assisted SAGIN systems that are capable of mitigating the detrimental effects of double-selectivity in the face of both time-varying ISI in the TD and the Doppler-induced ICI in the FD, resulting in a robust delay- and Doppler-resilient solution. The DD representation of the RIS-assisted SAGIN channels was devised, and the RIS was configured based on the statistical CSI in the DD-domain. Furthermore, an attractive DD channel estimation technique was conceived for RIS-assisted SAGINs, which is capable of supporting both OFDM and OTFS in a unified platform. Our simulation results demonstrate that the proposed OTFS-based RIS-assisted SAGIN systems are capable of achieving substantially improved performance over both the case of using only the direct link without RIS and the case of OFDM aided RIS

across a wide range of SAGIN channel parameters, including the Ricean K factor, Doppler frequency, delay spread, coverage distance and carrier frequency.

Nonetheless, it is worth noting that although it is proven in [66] from first principles that the DD-domain interferences induced by the fractional delay and Doppler indices become negligible, given sufficient time duration and bandwidth, many SAGIN applications rely on low-delay and low-rate communication links [1]–[7]. The potential DD-domain interferences imposed by the limited bandwidth for SAGIN control links exceed the scope of this paper and will be investigated in our future research.

## REFERENCES

- [1] S. Dang, O. Amin, B. Shihada, and M. Alouini, "What should 6G be?," *Nat. Electron.*, vol. 3, pp. 20–29, 2020.
- [2] X. You et al., "Towards 6G wireless communication networks: vision, enabling technologies, and new paradigm shifts," *Science China Inf. Sciences*, vol. 64, no. 110301, pp. 20–29, 2021.
- [3] F. Guo, F. Yu, H. Zhang, X. Li, H. Ji, and V. Leung, "Enabling massive IoT toward 6G: A comprehensive survey," *IEEE Internet Things J.*, vol. 8, no. 15, pp. 11891–11915, 2021.
- [4] D. Nguyen, M. Ding, P. Pathirana, A. Seneviratne, J. Li, D. Niyato, O. Dobre, and V. Poor, "6G internet of things: A comprehensive survey," *IEEE Internet Things J.*, vol. 9, no. 1, pp. 359–383, 2022.
- [5] C. Xu, N. Ishikawa, R. Rajashekar, S. Sugiura, R. G. Maunder, Z. Wang, L. Yang, and L. Hanzo, "Sixty years of coherent versus non-coherent tradeoffs and the road from 5G to wireless futures," *IEEE Access*, vol. 7, pp. 178246–178299, 2019.
- [6] L. Zhao, C. Wang, K. Zhao, D. Tarchi, S. Wan, and N. Kumar, "INTERLINK: A digital twin-assisted storage strategy for satellite-terrestrial networks," *IEEE Trans. Aerospace Electronic Syst.*, 2022.
- [7] M. Zhao, C. Chen, L. Liu, D. Lan, and S. Wan, "Orbital collaborative learning in 6g space-air-ground integrated networks," *Neurocomputing*, vol. 497, pp. 94–109, 2022.

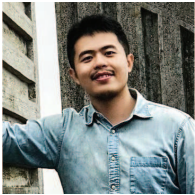
- [8] ITU *Measuring digital development: Facts and figures 2021* [Online]. Available: <https://www.itu.int/en/ITU-D/Statistics/Documents/facts/FactsFigures2021.pdf>.
- [9] IoT Analytics *State of the IoT 2020: 12 Billion IoT Connections, Surpassing Non-IoT for the First Time*. [Online]. Available: <https://iot-analytics.com/state-of-the-iot-2020-12-billion-iot-connections-surpassing-non-iot-for-the-first-time/>.
- [10] M. Shafi, A. Molisch, P. Smith, T. Haustein, P. Zhu, P. D. Silva, F. Tufvesson, A. Benjebbour, and G. Wunder, “5G: A tutorial overview of standards, trials, challenges, deployment, and practice,” *IEEE J. Sel. Areas Commun.*, vol. 35, no. 6, pp. 1201–1221, 2017.
- [11] A. Guidotti, A. Vanelli-Coralli, M. Conti, S. Andrenacci, S. Chatzinotas, N. Maturro, B. Evans, A. Awoseyila, A. Ugolini, T. Foggi, L. Gaudio, N. Alagha, and S. Cioni, “Architectures and key technical challenges for 5G systems incorporating satellites,” *IEEE Trans. Veh. Technol.*, vol. 68, no. 3, pp. 2624–2639, 2019.
- [12] B. Ai, A. Molisch, M. Rupp, and Z. Zhong, “5G key technologies for smart railways,” *Proc. IEEE*, vol. 108, no. 6, pp. 856–893, 2020.
- [13] L. Hanzo, Y. Akhtman, L. Wang, and M. Jiang, *MIMO-OFDM for LTE, WiFi and WiMAX: Coherent versus Non-coherent and Cooperative Turbo Transceivers*. John Wiley & Sons, 2011.
- [14] J. Zhang, L. Yang, L. Hanzo, and H. Gharavi, “Advances in cooperative single-carrier FDMA communications: Beyond LTE-advanced,” *IEEE Commun. Surveys Tuts.*, vol. 17, no. 2, pp. 730–756, 2015.
- [15] H. Nguyen, C. Xu, S. X. Ng, and L. Hanzo, “Near-capacity wireless system design principles,” *IEEE Commun. Surveys Tuts.*, vol. 17, no. 4, pp. 1806–1833, 2015.
- [16] R. Sun, D. W. Matolak, and W. Rayess, “Air-ground channel characterization for unmanned aircraft systems – Part IV: Airframe shadowing,” *IEEE Trans. Veh. Technol.*, vol. 66, pp. 7643–7652, Sept 2017.
- [17] J. Zhang, T. Chen, S. Zhong, J. Wang, W. Zhang, X. Zuo, R. G. Maunder, and L. Hanzo, “Aeronautical Ad Hoc networking for the internet-above-the-clouds,” *Proc. IEEE*, vol. 107, no. 5, pp. 868–911, 2019.
- [18] C. Xu, J. Zhang, T. Bai, P. Botsinis, R. G. Maunder, R. Zhang, and L. Hanzo, “Adaptive coherent/non-coherent single/multiple-antenna aided channel coded ground-to-air aeronautical communication,” *IEEE Trans. Commun.*, vol. 67, no. 2, pp. 1099–1116, 2019.
- [19] C. Xu, T. Bai, J. Zhang, R. Rajashekar, R. G. Maunder, Z. Wang, and L. Hanzo, “Adaptive coherent/non-coherent spatial modulation aided unmanned aircraft systems,” *IEEE Wireless Commun.*, vol. 26, no. 4, pp. 170–177, 2019.
- [20] S. Gong, X. Lu, D. T. Hoang, D. Niyato, L. Shu, D. I. Kim, and Y. Liang, “Towards smart wireless communications via intelligent reflecting surfaces: A contemporary survey,” *IEEE Commun. Surveys Tut.*, vol. 22, no. 4, pp. 2283–2314, 2020.
- [21] M. D. Renzo, A. Zappone, M. Debbah, M. Alouini, C. Yuen, J. de Rosny, and S. Tretyakov, “Smart radio environments empowered by reconfigurable intelligent surfaces: How it works, state of research, and the road ahead,” *IEEE J. Sel. Areas Commun.*, vol. 38, no. 11, pp. 2450–2525, 2020.
- [22] Q. Wu, S. Zhang, B. Zheng, S. You, and R. Zhang, “Intelligent reflecting surface-aided wireless communications: A tutorial,” *IEEE Trans. Commun.*, vol. 69, no. 5, pp. 3313–3351, 2021.
- [23] Y. Chen, Y. Wang, J. Zhang, and M. D. Renzo, “QoS-driven spectrum sharing for reconfigurable intelligent surfaces (RISs) aided vehicular networks,” *IEEE Trans. Wireless Commun.*, vol. 20, no. 9, pp. 5969–5985, 2021.
- [24] Y. Ai, F. deFigueiredo, L. Kong, M. Cheffena, S. Chatzinotas, and B. Ottersten, “Secure vehicular communications through reconfigurable intelligent surfaces,” *IEEE Trans. Veh. Technol.*, vol. 70, no. 7, pp. 7272–7276, 2021.
- [25] Y. Chen, Y. Wang, and L. Jiao, “Robust transmission for reconfigurable intelligent surface aided millimeter wave vehicular communications with statistical CSI,” *IEEE Trans. Wireless Commun.*, pp. 1–1, 2021.
- [26] A. Al-Hilo, M. Shokry, M. Elhattab, C. Assi, and S. Sharafeddine, “Reconfigurable intelligent surface enabled vehicular communication: Joint user scheduling and passive beamforming,” *IEEE Trans. Veh. Technol.*, 2022.
- [27] J. Xu and B. Ai, “When mmWave high-speed railway networks meet reconfigurable intelligent surface: A deep reinforcement learning method,” *IEEE Wireless Commun. Letts.*, 2021.
- [28] M. Gao, B. Ai, Y. Niu, Z. Han, and Z. Zhong, “IRS-assisted high-speed train communications: Outage probability minimization with statistical CSI,” in *ICC 2021 - IEEE Int. Conf. Commun.*, pp. 1–6, 2021.
- [29] M. Diamanti, P. Charatsaris, E. Tsiropoulou, and S. Papavassiliou, “The prospect of reconfigurable intelligent surfaces in integrated access and backhaul networks,” *IEEE Trans. Green Commun. Network.*, 2021.
- [30] S. Li, B. Duo, X. Yuan, Y. Liang, and M. D. Renzo, “Reconfigurable intelligent surface assisted UAV communication: Joint trajectory design and passive beamforming,” *IEEE Wireless Commun. Letts.*, vol. 9, no. 5, pp. 716–720, 2020.
- [31] M. Samir, M. Elhattab, C. Assi, S. Sharafeddine, and A. Ghayeb, “Optimizing age of information through aerial reconfigurable intelligent surfaces: A deep reinforcement learning approach,” *IEEE Trans. Veh. Technol.*, vol. 70, no. 4, pp. 3978–3983, 2021.
- [32] X. Liu, Y. Liu, and Y. Chen, “Machine learning empowered trajectory and passive beamforming design in UAV-RIS wireless networks,” *IEEE J. Sel. Areas Commun.*, vol. 39, no. 7, pp. 2042–2055, 2021.
- [33] L. Yang, F. Meng, J. Zhang, M. Hasna, and M. D. Renzo, “On the performance of RIS-assisted dual-hop UAV communication systems,” *IEEE Trans. Veh. Technol.*, vol. 69, no. 9, pp. 10385–10390, 2020.
- [34] Y. Pan, K. Wang, C. Pan, H. Zhu, and J. Wang, “UAV-assisted and intelligent reflecting surfaces-supported terahertz communications,” *IEEE Wireless Commun. Letts.*, vol. 10, no. 6, pp. 1256–1260, 2021.
- [35] S. Li, B. Duo, M. D. Renzo, M. Tao, and X. Yuan, “Robust secure UAV communications with the aid of reconfigurable intelligent surfaces,” *IEEE Trans. Wireless Commun.*, vol. 20, no. 10, pp. 6402–6417, 2021.
- [36] N. Agrawal, A. Bansal, K. Singh, and C. Li, “Performance evaluation of RIS-assisted UAV-enabled vehicular communication system with multiple non-identical interferers,” *IEEE Trans. Intelligent Transportation Syst.*, pp. 1–12, 2021.
- [37] K. Tekbiyik, G. Kurt, and H. Yanikomeroglu, “Energy-efficient ris-assisted satellites for IoT networks,” *IEEE Internet Things J.*, pp. 1–1, 2021.
- [38] J. Zhang and C. Qi, “Channel estimation for mmWave satellite communications with reconfigurable intelligent surface,” in *2021 IEEE Global Communications Conference (GLOBECOM)*, 2021.
- [39] K. Guo and K. An, “On the performance of RIS-assisted integrated satellite-UAV-terrestrial networks with hardware impairments and interference,” *IEEE Wireless Commun. Letts.*, vol. 11, no. 1, pp. 131–135, 2022.
- [40] S. Xu, J. Liu, Y. Cao, J. Li, and Y. Zhang, “Intelligent reflecting surface enabled secure cooperative transmission for satellite-terrestrial integrated networks,” *IEEE Trans. Veh. Technol.*, vol. 70, no. 2, pp. 2007–2011, 2021.
- [41] Y. Han, W. Tang, S. Jin, C. Wen, and X. Ma, “Large intelligent surface-assisted wireless communication exploiting statistical CSI,” *IEEE Trans. Veh. Technol.*, vol. 68, no. 8, pp. 8238–8242, 2019.
- [42] K. Ying, Z. Gao, S. Lyu, Y. Wu, H. Wang, and M. Alouini, “GMD-based hybrid beamforming for large reconfigurable intelligent surface assisted millimeter-wave massive MIMO,” *IEEE Access*, vol. 8, pp. 19530–19539, 2020.
- [43] B. Di, H. Zhang, L. Li, L. Song, Y. Li, and Z. Han, “Practical hybrid beamforming with finite-resolution phase shifters for reconfigurable intelligent surface based multi-user communications,” *IEEE Trans. Veh. Technol.*, vol. 69, no. 4, pp. 4565–4570, 2020.
- [44] J. He, H. Wymeersch, T. Sanguanpuak, O. Silven, and M. Juntti, “Adaptive beamforming design for mmWave RIS-aided joint localization and communication,” in *2020 IEEE Wireless Commun. Networking Conf. Workshops (WCNCW)*, pp. 1–6, 2020.
- [45] A. Taha, M. Alrabeiah, and A. Alkhateeb, “Enabling large intelligent surfaces with compressive sensing and deep learning,” *IEEE Access*, vol. 9, pp. 44304–44321, 2021.
- [46] S. Liu, Z. Gao, J. Zhang, M. D. Renzo, and M.-S. Alouini, “Deep denoising neural network assisted compressive channel estimation for mmWave intelligent reflecting surfaces,” *IEEE Trans. Veh. Technol.*, vol. 69, no. 8, pp. 9223–9228, 2020.
- [47] G. C. Alexandropoulos and E. Vlachos, “A hardware architecture for reconfigurable intelligent surfaces with minimal active elements for explicit channel estimation,” in *IEEE Int. Conf. Acoustics, Speech Signal Process. (ICASSP)*, pp. 9175–9179, 2020.
- [48] Y. Yang, B. Zheng, S. Zhang, and R. Zhang, “Intelligent reflecting surface meets OFDM: Protocol design and rate maximization,” *IEEE Trans. Commun.*, vol. 68, no. 7, pp. 4522–4535, 2020.
- [49] Z. Wang, L. Liu, and S. Cui, “Channel estimation for intelligent reflecting surface assisted multiuser communications: Framework, algorithms, and analysis,” *IEEE Trans. Wireless Commun.*, pp. 1–1, 2020.
- [50] T. L. Jensen and E. De Carvalho, “An optimal channel estimation scheme for intelligent reflecting surfaces based on a minimum variance unbiased estimator,” in *IEEE Int. Conf. Acoustics, Speech Signal Process. (ICASSP)*, pp. 5000–5004, 2020.
- [51] B. Zheng and R. Zhang, “Intelligent reflecting surface-enhanced OFDM: Channel estimation and reflection optimization,” *IEEE Wireless Commun. Letts.*, vol. 9, no. 4, pp. 518–522, 2020.

- [52] Q. Nadeem, H. Alwazani, A. Kammoun, A. Chaaban, M. Debbah, and M. Alouini, "Intelligent reflecting surface-assisted multi-user MISO communication: Channel estimation and beamforming design," *IEEE Open J. the Commun. Society*, vol. 1, pp. 661–680, 2020.
- [53] Z. He and X. Yuan, "Cascaded channel estimation for large intelligent metasurface assisted massive mimo," *IEEE Wireless Commun. Lett.*, vol. 9, no. 2, pp. 210–214, 2020.
- [54] H. Liu, X. Yuan, and Y. A. Zhang, "Matrix-calibration-based cascaded channel estimation for reconfigurable intelligent surface assisted multiuser MIMO," *IEEE J. Sel. Areas Commun.*, pp. 1–1, 2020.
- [55] L. Wei, C. Huang, G. C. Alexandropoulos, and C. Yuen, "Parallel factor decomposition channel estimation in RIS-assisted multi-user MISO communication," in *2020 IEEE 11th Sensor Array and Multichannel Signal Processing Workshop (SAM)*, pp. 1–5, 2020.
- [56] L. Wei, C. Huang, G. C. Alexandropoulos, C. Yuen, Z. Zhang, and M. Debbah, "Channel estimation for RIS-empowered multi-user MISO wireless communications," *IEEE Trans. Commun.*, vol. 69, no. 6, pp. 4144–4157, 2021.
- [57] B. Xiong, Z. Zhang, H. Jiang, J. Zhang, L. Wu, and J. Dang, "A 3D non-stationary MIMO channel model for reconfigurable intelligent surface auxiliary UAV-to-ground mmWave communications," *IEEE Trans. Wireless Commun.*, 2022.
- [58] C. Xu, J. An, T. Bai, L. Xiang, S. Sugiura, R. Maunder, L. Yang, and L. Hanzo, "Reconfigurable intelligent surface assisted multi-carrier wireless systems for doubly selective high-mobility rician channels," *IEEE Trans. Veh. Technol.*, vol. 71, no. 4, pp. 4023–4041, 2022.
- [59] C. You, B. Zheng, and R. Zhang, "Channel estimation and passive beamforming for intelligent reflecting surface: Discrete phase shift and progressive refinement," *IEEE J. Sel. Areas Commun.*, 2020.
- [60] C. You, B. Zheng, and R. Zhang, "Progressive channel estimation and passive beamforming for intelligent reflecting surface with discrete phase shifts," *arXiv preprint arXiv:1912.10646*.
- [61] P. Wang, J. Fang, H. Duan, and H. Li, "Compressed channel estimation for intelligent reflecting surface-assisted millimeter wave systems," *IEEE Signal Process. Lett.*, vol. 27, pp. 905–909, 2020.
- [62] J. Chen, Y.-C. Liang, H. V. Cheng, and W. Yu, "Channel estimation for reconfigurable intelligent surface aided multi-user MIMO systems," *arXiv preprint arXiv:1912.03619*.
- [63] X. Ma, Z. Chen, W. Chen, Z. Li, Y. Chi, C. Han, and S. Li, "Joint channel estimation and data rate maximization for intelligent reflecting surface assisted terahertz MIMO communication systems," *IEEE Access*, pp. 99565–99581, 2020.
- [64] R. Hadani, S. Rakib, M. Tsatsanis, A. Monk, A. Goldsmith, A. Molisch, and R. Calderbank, "Orthogonal time frequency space modulation," in *2017 IEEE Wireless Communications and Networking Conference (WCNC)*, pp. 1–6, 2017.
- [65] Z. Wei, W. Yuan, S. Li, J. Yuan, G. Bharatula, R. Hadani, and L. Hanzo, "Orthogonal time-frequency space modulation: A promising next-generation waveform," *IEEE Wireless Commun.*, vol. 28, no. 4, pp. 136–144, 2021.
- [66] S. Mohammed, "Derivation of OTFS modulation from first principles," *IEEE Trans. Veh. Technol.*, vol. 70, no. 8, pp. 7619–7636, 2021.
- [67] A. Farhang, A. RezaezadehReyhani, L. Doyle, and B. Farhang-Boroujeny, "Low complexity modem structure for OFDM-based orthogonal time frequency space modulation," *IEEE Wireless Commun. Lett.*, vol. 7, no. 3, pp. 344–347, 2018.
- [68] P. Raviteja, Y. Hong, E. Viterbo, and E. Biglieri, "Practical pulse-shaping waveforms for reduced-cyclic-prefix OTFS," *IEEE Trans. Veh. Technol.*, vol. 68, no. 1, pp. 957–961, 2019.
- [69] Z. Wei, W. Yuan, S. Li, J. Yuan, and D. Ng, "Transmitter and receiver window designs for orthogonal time-frequency space modulation," *IEEE Trans. Commun.*, vol. 69, no. 4, pp. 2207–2223, 2021.
- [70] G. Surabhi, R. Augustine, and A. Chockalingam, "On the diversity of uncoded OTFS modulation in doubly-dispersive channels," *IEEE Trans. Wireless Commun.*, vol. 18, no. 6, pp. 3049–3063, 2019.
- [71] P. Raviteja, Y. Hong, E. Viterbo, and E. Biglieri, "Effective diversity of OTFS modulation," *IEEE Wireless Commun. Lett.*, vol. 9, no. 2, pp. 249–253, 2020.
- [72] S. Li, J. Yuan, W. Yuan, Z. Wei, B. Bai, and D. Ng, "Performance analysis of coded OTFS systems over high-mobility channels," *IEEE Trans. Wireless Commun.*, vol. 20, no. 9, pp. 6033–6048, 2021.
- [73] P. Raviteja, K. T. Phan, and Y. Hong, "Embedded pilot-aided channel estimation for OTFS in delay-doppler channels," *IEEE Trans. Veh. Technol.*, vol. 68, no. 5, pp. 4906–4917, 2019.
- [74] W. Shen, L. Dai, J. An, P. Fan, and R. Heath, "Channel estimation for orthogonal time frequency space (OTFS) massive MIMO," *IEEE Trans. Signal Process.*, vol. 67, no. 16, pp. 4204–4217, 2019.
- [75] S. Tiwari, S. Das, and V. Rangamgari, "Low complexity LMMSE receiver for OTFS," *IEEE Commun. Lett.*, vol. 23, no. 12, pp. 2205–2209, 2019.
- [76] G. Surabhi and A. Chockalingam, "Low-complexity linear equalization for OTFS modulation," *IEEE Commun. Lett.*, vol. 24, no. 2, pp. 330–334, 2020.
- [77] P. Raviteja, K. Phan, Y. Hong, and E. Viterbo, "Interference cancellation and iterative detection for orthogonal time frequency space modulation," *IEEE Trans. Wireless Commun.*, vol. 17, no. 10, pp. 6501–6515, 2018.
- [78] W. Yuan, Z. Wei, J. Yuan, and D. Ng, "A simple variational Bayes detector for orthogonal time frequency space (OTFS) modulation," *IEEE Trans. Veh. Technol.*, vol. 69, no. 7, pp. 7976–7980, 2020.
- [79] L. Xiang, Y. Liu, L. Yang, and L. Hanzo, "Gaussian approximate message passing detection of orthogonal time frequency space modulation," *IEEE Trans. Veh. Technol.*, vol. 70, no. 10, pp. 10999–11004, 2021.
- [80] A. Abrardo, D. Dardari, and M. D. Renzo, "Intelligent reflecting surfaces: Sum-rate optimization based on statistical position information," *IEEE Trans. Commun.*, vol. 69, no. 10, pp. 7121–7136, 2021.
- [81] X. Gan, C. Zhong, C. Huang, and Z. Zhang, "RIS-assisted multi-user MISO communications exploiting statistical CSI," *IEEE Trans. Commun.*, vol. 69, no. 10, pp. 6781–6792, 2021.
- [82] K. Zhi, C. Pan, H. Ren, and K. Wang, "Statistical CSI-based design for reconfigurable intelligent surface-aided massive MIMO systems with direct links," *IEEE Wireless Commun. Lett.*, vol. 10, no. 5, pp. 1128–1132, 2021.
- [83] Z. Shi, H. Wang, Y. Fu, G. Yang, S. Ma, and F. Gao, "Outage analysis of reconfigurable intelligent surface aided MIMO communications with statistical CSI," *IEEE Trans. Wireless Commun.*, vol. 21, no. 2, pp. 823–839, 2022.
- [84] R. Steele and L. Hanzo, *Mobile Radio Communications*. John Wiley & Sons, May 1999.
- [85] J. G. Proakis, *Digital Communications*. New York: McGraw-Hill, 1995.
- [86] A. Goldsmith, *Wireless communications*. Cambridge University Press, 2005.
- [87] L. Hanzo, O. Alamri, M. El-Hajjar, and N. Wu, *Near-Capacity Multi-Functional MIMO Systems: Sphere-Packing, Iterative Detection and Cooperation*. John Wiley & Sons, May 2009.
- [88] I. A. Hemadeh, K. Satyanarayana, M. El-Hajjar, and L. Hanzo, "Millimeter-wave communications: Physical channel models, design considerations, antenna constructions, and link-budget," *IEEE Commun. Surveys Tut.*, vol. 20, pp. 870–913, Secondquarter 2018.
- [89] T. S. Rappaport, Y. Xing, O. Kanhere, S. Ju, A. Madanayake, S. Mandal, A. Alkhateeb, and G. C. Trichopoulos, "Wireless communications and applications above 100 GHz: Opportunities and challenges for 6G and beyond," *IEEE Access*, 2019.
- [90] O. Ozdogan, E. Bjornson, and E. G. Larsson, "Intelligent reflecting surfaces: Physics, propagation, and pathloss modeling," *IEEE Wireless Commun. Lett.*, vol. 9, no. 5, pp. 581–585, 2020.
- [91] W. Tang, M. Z. Chen, X. Chen, J. Y. Dai, Y. Han, M. D. Renzo, Y. Zeng, S. Jin, Q. Cheng, and T. J. Cui, "Wireless communications with reconfigurable intelligent surface: Path loss modeling and experimental measurement," *IEEE Trans. Wireless Commun.*, vol. 20, no. 1, pp. 421–439, 2021.
- [92] J. Garcia, A. Sibille, and M. Kamoun, "Reconfigurable intelligent surfaces: Bridging the gap between scattering and reflection," *IEEE J. Sel. Areas Commun.*, vol. 38, no. 11, pp. 2538–2547, 2020.
- [93] C. Xu, S. Sugiura, S. X. Ng, P. Zhang, L. Wang, and L. Hanzo, "Two decades of MIMO design tradeoffs and reduced-complexity MIMO detection in near-capacity systems," *IEEE Access*, vol. 5, pp. 18564–18632, 2017.

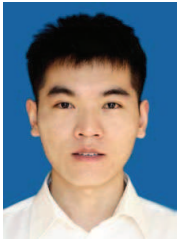


**Chao Xu** (S'09-M'14-SM'19) received a B.Eng. degree from Beijing University of Posts and Telecommunications, China, and a BSc(Eng) with First Class Honours from Queen Mary, University of London, UK, through a Sino-UK joint degree program in 2008, both in Telecommunications. He obtained a MSc degree with distinction in Radio Frequency Communication Systems and a Ph.D. degree in Wireless Communications from the University of Southampton, UK in 2009 and 2015, respectively. He is currently a senior research fellow working at

Next Generation Wireless Research Group, University of Southampton, UK. His research interests include index modulation, reconfigurable intelligent surfaces, noncoherent detection and turbo detection. He was awarded the Best M.Sc. Student in Broadband and Mobile Communication Networks by the IEEE Communications Society (United Kingdom and Republic of Ireland Chapter) in 2009. He also received 2012 Chinese Government Award for Outstanding Self-Financed Student Abroad and 2017 Dean's Award, Faculty of Physical Sciences and Engineering, the University of Southampton.



**Luping Xiang** received the B.Eng. degree (Hons.) from Xiamen University, China, in 2015, and the Ph.D. degree from the University of Southampton, in 2020. From 2020 to 2021 He was a Research Fellow with the Next Generation Wireless Group, University of Southampton. He began a lectureship in November 2021 at School of Information and Communication Engineering, University of Electronic Science and Technology of China. His research interests include machine learning, channel coding and modulation/demodulation.



**Jiancheng An** received the B.S. degree in Electronics and Information Engineering and the Ph.D. degree in Information and Communication Engineering from the University of Electronic Science and Technology of China (UESTC), Chengdu, China, in 2016 and 2021, respectively. From 2019 to 2020, he was a Visiting Scholar with the Next-Generation Wireless Group, University of Southampton, U.K. He is currently a research fellow with the Engineering Product Development (EPD) Pillar, Singapore University of Technology and Design (SUTD). His

research interests include integrated sensing and communications (ISAC), reconfigurable intelligent surfaces (RIS), and holographic MIMO.



**Chen Dong** received the B.S. degree in electronic information sciences and technology from the University of Science and Technology of China, Hefei, China, in 2004, the M.Eng. degree in pattern recognition and automatic equipment from the University of Chinese Academy of Sciences, Beijing, China, in 2007, and the Ph.D. degree from the University of Southampton, U.K., in 2014. After the post-doc experience in Southampton, he used to work in Huawei Device Co., Ltd., China. Since 2020, he works with Beijing University of Posts and Telecom-

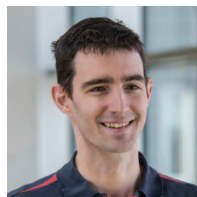
munications(BUPT). His research interests include applied math, relay system, channel modeling, and cross-layer optimization. He was a recipient of the Scholarship under the U.K.-China Scholarships for Excellence Programme and the Best Paper Award at the IEEE VTC 2014.



**Shinya Sugiura** (M'06-SM'12) received the B.S. and M.S. degrees in aeronautics and astronautics from Kyoto University, Kyoto, Japan, in 2002 and 2004, respectively, and the Ph.D. degree in electronics and electrical engineering from the University of Southampton, Southampton, U.K., in 2010.

From 2004 to 2012, he was a Research Scientist with Toyota Central Research and Development Laboratories, Inc., Nagakute, Japan. From 2013 to 2018, he was an Associate Professor with the Department of Computer and Information Sciences, Tokyo University of Agriculture and Technology, Koganei, Japan. Since 2018, he has been an Associate Professor with the Institute of Industrial Science, The University of Tokyo, Tokyo, Japan, where he heads the Wireless Communications Research Group. In 2019, he was recognized as The University of Tokyo Excellent Young Researcher. His research has covered a range of areas in wireless communications, networking, signal processing, and antenna technology. He authored or coauthored over 90 IEEE journal papers.

Dr. Sugiura was a recipient of numerous awards, including the 18th JSPS Prize in 2022, the Fifth Yasuharu Suematsu Award in 2019, the Sixth RIEC Award from the Foundation for the Promotion of Electrical Communication in 2016, the Young Scientists' Prize by the Minister of Education, Culture, Sports, Science and Technology of Japan in 2016, the 14th Funai Information Technology Award (First Prize) from the Funai Foundation in 2015, the 28th Telecom System Technology Award from the Telecommunications Advancement Foundation in 2013, the Sixth IEEE Communications Society Asia-Pacific Outstanding Young Researcher Award in 2011, the 13th Ericsson Young Scientist Award in 2011, and the 2008 IEEE Antennas and Propagation Society Japan Chapter Young Engineer Award. He has served as an Editor for IEEE WIRELESS COMMUNICATIONS LETTERS since 2019 and as an Editor for SCIENTIFIC REPORTS since 2021. He was certified as an Exemplary Editor for IEEE WIRELESS COMMUNICATIONS LETTERS in 2020, as an Exemplary Reviewer for IEEE COMMUNICATIONS LETTERS in 2013 and 2014, and as an Exemplary Reviewer for IEEE TRANSACTIONS ON COMMUNICATIONS in 2018.



**Prof Robert G. Maunder** has studied with the School of Electronics and Computer Science, University of Southampton, UK, since October 2000. He was awarded a first class honours BEng in Electronic Engineering in July 2003, as well as a PhD in Telecommunications in December 2007. He began a lectureship in November 2007 and was promoted to Associate Professor in March 2013 and to Professor in August 2017. He was awarded Senior Member status of the IEEE in December 2012, Chartered Engineer status of the IET in November 2013 and

Fellow status of the IET in January 2017. Rob's research interests include joint source/channel coding and the holistic design of algorithms and hardware implementations for wireless communications. He has published a number of IEEE papers in these areas. He is the founder and CTO of AccelerComm Ltd, which is commercialising his research as soft-IP.



**Lie-Liang Yang (M'98, SM'02, F'16)** received his BEng degree in communications engineering from Shanghai TieDao University, Shanghai, China in 1988, and his MEng and PhD degrees in communications and electronics from Northern (Beijing) Jiaotong University, Beijing, China in 1991 and 1997, respectively. From June 1997 to December 1997, he was a visiting scientist to the Institute of Radio Engineering and Electronics, Academy of Sciences of the Czech Republic. Since December 1997, he has been with the University of Southampton,

United Kingdom, where he is the professor of Wireless Communications in the School of Electronics and Computer Science. He has research interest in wireless communications, wireless networks and signal processing for wireless communications, as well as molecular communications and nano-networks. He has published 400+ research papers in journals and conference proceedings, authored/co-authored three books and also published several book chapters. The details about his research publications can be found at <https://www.ecs.soton.ac.uk/people/llyang>. He is a fellow of both the IEEE and the IET, and was a distinguished lecturer of the IEEE VTS. He served as an associate editor to the IEEE Trans. on Vehicular Technology and Journal of Communications and Networks (JCN), and is currently a senior editor to the IEEE Access and a subject editor to the Electronics Letters.



**Lajos Hanzo** (<http://www-mobile.ecs.soton.ac.uk>, [https://en.wikipedia.org/wiki/Lajos\\_Hanzo](https://en.wikipedia.org/wiki/Lajos_Hanzo))

(FIEEE'04) received his Master degree and Doctorate in 1976 and 1983, respectively from the Technical University (TU) of Budapest. He was also awarded the Doctor of Sciences (DSc) degree by the University of Southampton (2004) and Honorary Doctorates by the TU of Budapest (2009) and by the University of Edinburgh (2015). He is a Foreign Member of the Hungarian Academy of Sciences and a former Editor-in-Chief of the IEEE

Press. He has served several terms as Governor of both IEEE ComSoc and of VTS. He has published 2000+ contributions at IEEE Xplore, 19 Wiley-IEEE Press books and has helped the fast-track career of 123 PhD students. Over 40 of them are Professors at various stages of their careers in academia and many of them are leading scientists in the wireless industry. He is also a Fellow of the Royal Academy of Engineering (FREng), of the IET and of EURASIP. He holds the Eric Sumner Field Award.